Medizinische Fakultät

Nuklearmedizin

Optimierungsstrategien für paraCEST Kontrastmittel in der Magnetresonanztomographie

Giaime Rancan

Vollständiger Abdruck der von der Fakultät für Medizin der Technischen Universität München zur Erlangung des akademischen Grades eines Doktors der Naturwissenschaften genehmigten Dissertation.

Vorsitzende(r): Univ. -Prof. Dr. M. J. Atkinson

Prüfer der Dissertation:

1. Univ. -Prof. Dr. M. Schwaiger
2. Univ. -Prof. Dr. S. J. Glaser

Die Dissertation wurde am 19.05.2015 bei der Technischen Universität München eingereicht und durch die Fakultät für Medizin am 16.09.2015 angenommen.

Technische Universität München

PhD Thesis

Optimization Strategies for ParaCEST Contrast Agents in MRI

Giaime Rancan

May 2015

First Supervisor: Prof. M. Schwaiger
Second Supervisor: Prof. S. Glaser
Mentor: Prof. S. Aime

Contents

Foreword v
1 Introduction v

1 State-of-the-art 1
1.1 Magnetization Transfer 1
1.2 Chemical Exchange Saturation Transfer 3
1.3 CEST and other shifted chemical exchange (SCE) techniques 7
1.4 CEST contrast agents 8
1.5 In vivo CEST 9
1.6 pH imaging and Ratiometric analysis 10
1.7 The $R_{1\rho}$ formalism in CEST 13
1.8 ParaCEST contrast agents 15
1.9 Preclinical applications 17
1.10 Clinical applications 18
1.11 MRI sequences for CEST 20

2 MRI CEST at 1T with large μ_{eff} Ln^{3+} complexes. Tm^{3+}-HPDO3A: an efficient MRI pH reporter. 23

3 Gradient Ascent Pulse Engineering for Rapid Exchange Saturation Transfer 33

4 Liposomial drug delivery system: characterization of encapsulated Yb-HPDO3A 43
4.1 Introduction 43
4.2 Methods 44
4.3 Results 44
4.4 Discussion and conclusions 47

A On the Bloch equation 49

B Summary on: MRI CEST at 1T with large μ_{eff} Ln^{3+} complexes. Tm^{3+}-HPDO3A: an efficient MRI pH reporter. 53

C Summary on: Gradient Ascent Pulse Engineering for Rapid Exchange Saturation Transfer 55

Bibliography 57

Afterword 63

Foreword

1 Introduction

The field of nuclear magnetic resonance (NMR) is vast, with applications ranging from chemical analysis to magnetic resonance imaging (MRI). Medical applications have embraced this imaging modality for its safety and diagnostic power. Among the advantages of MRI is the variety of molecular imaging techniques that it offers. These may employ contrast media for added diagnostic value. Studying the complexity of selected tissues of interest, such as solid tumors, may require the use of equally complex imaging techniques and carefully designed contrast agents. In this document, the focus will be on a particular molecular imaging technique: chemical exchange saturation transfer employing paramagnetic contrast agents (paraCEST).

The present document is to be understood as a step in the translational effort of paraCEST contrast agents from preclinical to clinical applications. The document has been written following the guidelines for a cumulative thesis, and is composed of a state-of-the-art introduction, two standalone chapters (accepted in their current form as full papers in peer-reviewed journals), and an additional chapter presenting work yet to be approved for publication. A summary of each paper can be found in the appendix.

The projects included herein have received funding from the TUM-IAS (Institute for Advanced Study) and the SFB-DFG (Sonderforschungsbereiche der Deutschen Forschungsgemeinschaft). The author acknowledges all co-authors for their essential scientific support, as well as the colleagues listed in the afterword for moral and/or technical support.

Chapter 1

State-of-the-art

1.1 Magnetization Transfer

See review by Henkelmann et al. (2001)(1).

Magnetization transfer (MT) in MRI is a technique used to generate contrast by decreasing the water signal intensity in a spin density experiment, while avoiding direct water saturation. MT-MRI was first presented by Wolff and Balaban (2) and has since been used for clinical imaging, as well as paving the way to related chemical exchange saturation transfer (CEST) imaging modalities. Although conceptually overlapping, the two techniques are different in scope and applications.

MT allows indirect saturation of the water pool through nonshifted tissutal macromolecules. These are oftentimes present in abundance in the imaged tissues. The macromolecules are bound to water, thereby decreasing this spin pool's T_2 to the order of microseconds (3), and causing their absorption lineshape to be broadened. By applying an offresonant (with respect to both free and bound water pools) RF pulse, the bound water may be saturated. The free water may also be directly saturated by the offresonant irradiation, which is commonly referred to as spillover effect. Either contributions to the water signal intensity depend on the pulse's characteristics (offset, bandwidth and amplitude), as well as the proton pools' absorption lineshapes. Since the bound water is involved in an exchange with the free water, part of the saturation from each pool will be transferred to the other. The transfer can be an actual positional transfer of a saturated proton, or can take place through dipolar coupling (4). Recent literature (5) refers to this second contribution as nuclear overhauser effect (NOE), additionally distinguishing between direct and exchange relayed NOE. NOE effects are observed in vivo at +1 to +4 ppm (coupling with aromatic protons) (6) and especially between -2 to -5 ppm (with aliphatic protons) from water, making the contributions irrelevant for highly shifted CEST effects, among which paraCEST.

Both MT and NOE contributions can be modeled through the Bloch equations (7)(Appendix A). The treatment of macromolecular MT is analogous to the one

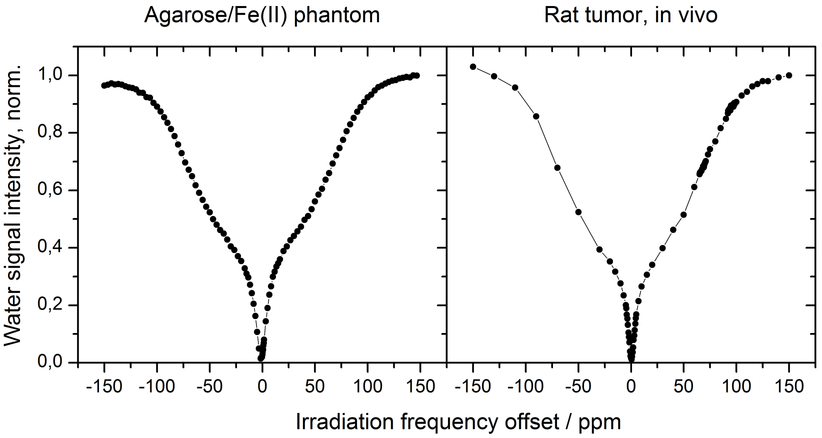

Figure 1.1: Z spectra (plot of the water signal intensity after a sweep of presaturation frequencies) acquired in the ± 150 ppm frequency range after a 4 s continuous wave presaturation of 320 Hz amplitude. The spectrum on the right shows the MT response from a subcutaneous solid tumor. The spectrum on the left is obtained from a phantom containing 3% agarose, 20 mM $FeSO_4$ (stabilized with 60 mM citrate and 50 mM ascorbate to prevent oxidation). The phantom demonstrates a large, immobilized proton pool with a short T_2 induced by the paramagnetic Iron(II).

performed for chemical exchange (8). The transverse components of the MT pool are assumed to be negligible, as the T_2 times are in the order of μs. In addition, the lineshape of the macromolecular pool is considered by the relaxation term R^{MT}, defined as:

$$R_b^{MT}(\Delta\omega) = g_b(\Delta\omega)\omega_1^2\pi$$

where $\Delta\omega$ is the irradiation frequency offset relative to the pool's Larmor frequency, ω_1 the amplitude of the irradiating RF field, and

$$g_b(\Delta\omega) = \frac{T_2}{\pi(1 + (\Delta\omega \cdot T_2)^2)}$$

In practice, the choice of the lineshape depends on the best experimental fit to the largely symmetric MT effect. Lineshapes are typically gaussian (common for solid pools), lorentzian (for liquid pools) and super-lorentzian (for semi-solid pools) (9). The effect of MT in a broad offset frequency range can be seen in Figure 1.1.

The time evolution of the magnetization vector can be described as follows:

$$\dot{\mathbf{M}} = A\mathbf{M}$$

$$A = \begin{pmatrix} 0 & 0 & 0 & 0 & 0 \\ 0 & -R_{2a} & -\Delta\omega_a & \omega_2 & 0 \\ 0 & \Delta\omega_a & -R_{2a} & -\omega_1 & 0 \\ M_{0a}R_{1a} & -\omega_2 & \omega_1 & -R_{1a} - C_{ab} & C_{ba} \\ M_{0b}R_{1b} & 0 & 0 & C_{ab} & -R_{1b} - C_{ba} - R_b^{MT} \end{pmatrix}$$

$$\mathbf{M} = \begin{pmatrix} 1 \\ M_x^a \\ M_y^a \\ M_z^a \\ M_z^b \end{pmatrix}$$

Where R_{1n} and R_{2n} are the longitudinal and transversal relaxation rates for the exchanging proton pool n (a is the free, b the bound proton pool)). $\Delta\omega_a$ is the frequency offset between the irradiating RF field and the water Larmor frequency. M_{0n} is the pools' equilibrium magnetization and C_n the exchange rate adjusted for relative concentration. $M^n_{x,y,z}$ are the components of the magnetization vector for pool n. ω_1 and ω_2 represent the x and y components of the irradiating RF field (for a treatment of the Bloch equations, see Appendix A).

With the acronym CEST, a particular technique is intended that employs the sole positional transfer to generate contrast, but does so through proton pools the absorption lineshape of which is shifted with respect to the water Larmor frequency. Therefore, while both MT and CEST generate negative contrast in the water signal by means of off-resonant RF irradiation, the contribution from CEST is asymmetrical. Moreover, the proton exchange in CEST is not between two water pools, but between the hydrogen spins of water and those covalently bound to a CEST molecule. Generally, the absorption lineshape of a CEST pool is also considerably more narrow, with longer T_2 times involved.

1.2 Chemical Exchange Saturation Transfer

See review by Zaiss and Bachert (2013)(7).

Chemical Exchange Saturation Transfer (CEST) (10) is a technique that exploits the spin exchange in molecules with chemical shifts different from water. This exchange is commonly between a proton-dense pool (e.g. water in living tissues) and a directly undetectable, chemically shifted, low-concentration spin pool (e.g.

from contrast media or endogenous biomolecules). By irradiation of the shifted proton pool, saturation is transferred to the observed proton-rich pool, where it accumulates up to a steady state. The technique generates an indirect saturation of the observed pool that follows the rules of spin diffusion and exchange. The effect can be modeled with good approximation by the Bloch equations modified for chemical exchange:

$$\dot{\mathbf{M}} = A\mathbf{M}$$

$$A = \begin{pmatrix} 0 & 0 & 0 & 0 & 0 & 0 & 0 \\ 0 & -R_{2a} - C_{ab} & -\Delta\omega_a & \omega_2 & C_{ba} & 0 & 0 \\ 0 & \Delta\omega_a & -R_{2a} - C_{ab} & -\omega_1 & 0 & C_{ba} & 0 \\ M_{0a}R_{1a} & -\omega_2 & \omega_1 & -R_{1a} - C_{ab} & 0 & 0 & C_{ba} \\ 0 & C_{ab} & 0 & 0 & -R_{2b} - C_{ba} & -\Delta\omega_b & \omega_2 \\ 0 & 0 & C_{ab} & 0 & \Delta\omega_b & -R_{2b} - C_{ba} & -\omega_1 \\ M_{0b}R_{1b} & 0 & 0 & C_{ab} & -\omega_2 & \omega_1 & -R_{1b} - C_{ba} \end{pmatrix}$$

$$\mathbf{M} = \begin{pmatrix} 1 \\ M_x^a \\ M_y^a \\ M_z^a \\ M_x^b \\ M_y^b \\ M_z^b \end{pmatrix}$$

which differ from the previously treated MT modeling by the inclusion of the transverse component of the CEST pool b, and the relevant exchange parameters.

A typical CEST experiment involves measuring the observed pool's signal magnitude after a sweep of irradiation frequencies. Its graphical representation is called a Z spectrum (Figure 1.1 and 1.2). The Z value is offset dependent and defined as:

$$Z(\Delta\omega) = M_z^a / M_0^a$$

where M_z^a is the residual Z magnetization of the observed water pool after saturation and M_0^a is the initial longitudinal magnetization (obtained from a reference scan). The on-resonance frequency of the observed pool is set to $\Delta\omega = 0$ by convention.

The generation of negative contrast through CEST involves a multitude of parameters, both internal to the observed chemical system (chemical shift, T_1, T_2,

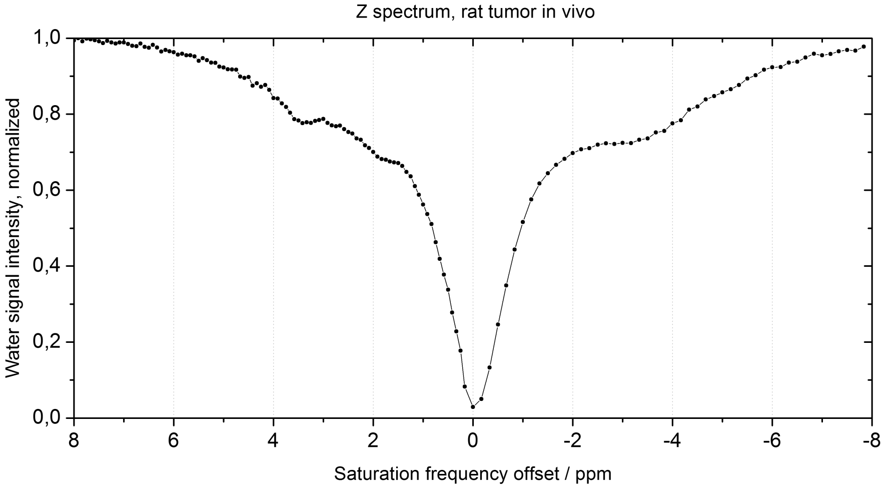

Figure 1.2: Z spectrum obtained from a single voxel of a subcutaneous solid tumor (mammary carcinoma, 13762 MAT B III) in a live Fischer 344 rat. Voxel size: 0.47x0.47x1.0 mm, 4 s *cw*-saturation of 139 Hz amplitude. At the direct water saturation (Offset = 0 ppm) the signal is at the minimum. Saturation symmetrical to the water frequency can be ascribed to MT and spillover contibutions. Between -2 and -5 ppm, NOE produces a reduction in the water signal intensity. At +2 and +3.5 ppm offset the signals from endogenous CEST contributions (of macromolecular amines and amides respectively) can be seen. Not present in this voxel is the peak from fat saturation (ca. -3.4 ppm), which can distort the NOE signal. Additional endogenous (depending on the tissue of interest) and exogenous (depending on contrast agent biodistribution) CEST signals can be detected on a Z spectrum.

exchange rates, spin concentration) and external to it (irradiation rf pulses, B_0, SAR limits, field inhomogeneities and hardware specifications). The relationships between the named parameters can be understood through numerical simulations or in simplified steady state conditions, which provide useful insight.

The chemical shift of the exchanging pools is a main limiting factor in CEST. It determines the maximum rate of the chemical exchange that can be observed before the exchanging pools become indistinguishable. To avoid the fast exchange limit, the frequency separation is required to be much higher than the exchange rate ($\Delta\omega >> k_{ex}$). The labeling efficiency (α) has been used as a parameter to determine a system's optimal operating conditions ((11)(12)), by defining the yield of the saturation transfer. The figure α is both offset and amplitude-dependent, and in its most general form can be represented by:

$$\alpha(\Delta\omega, \omega_1) = \frac{\delta\omega_b^2}{\omega_1^2 + \Delta\omega^2}(1 + \frac{R_{2b}}{k_b}\frac{\omega_1^2}{\Delta\omega^2 + 0.25 \cdot \Gamma^2})$$

where $\Delta\omega$ is the irradiation offset, ω_1 the irradiation amplitude, $\delta\omega_b$ is the offset of pool b, R_{2b} the transversal relaxation rate for that pool, and k_b its exchange rate. Γ is the lineshape of the proton pool ST signal.

On resonance on pool b, the labeling efficiency is:

$$\alpha = \frac{\frac{\delta\omega_b^2}{\omega_1^2+\delta\omega_b^2}k_b + R_{2b}}{k_b + R_{2b}}\frac{\omega_1^2}{\omega_1^2 + k_b(k_b + R_{2b})}$$

And in the large shift limit ($\delta\omega_b >> \omega_1$), is reduced to:

$$\alpha_{LS} = \frac{\omega_1^2}{\omega_1^2 + k_b(k_b + R_{2b})}$$

This figure is very important to understand optimal CEST conditions. It underlines the advantages of high chemical shifts (consider the large shift limit). For high exchange (k_b) and relaxation (R_{2b}) rates, the saturation amplitude needs to be comparably high to achieve good labeling efficiency. This can be understood intuitively by considering that very short residence times on the CEST molecules mean that a spin will only experience a fraction of the irradiating RF pulse. Practically, it means that instrumental specifications (e.g. RF power amplifier) and SAR limits become crucial for certain systems - as is the case for most paraCEST complexes.

A second limiting factor is saturation spillover, i.e. the amount of direct saturation obtained on the observed pool when the irradiation pulse is off-resonance. From the single pool Bloch equations, irradiation in steady state can be represented by the lorentzian line of direct water saturation:

$$\frac{M_Z}{M_0} = \frac{1}{1 + \frac{\omega_1^2 T_1 T_2}{1+\Delta\omega^2 T_2^2}} = \frac{R_1(R_2^2 + \Delta\omega^2)}{R_1(R_2^2 + \Delta\omega^2) + \omega_1^2 R_2}$$

The spillover effect can be elegantly described using the R_{eff} component of $R_{1\rho}$, the longitudinal relaxation rate of water in the rotating frame (Section 1.7). $R_{1\rho}$ is affected by the irradiating field, as well as by chemical exchange and MT.

1.3 CEST and other shifted chemical exchange (SCE) techniques

The techniques treated in this section represent the multiple strategies that can be followed to detect shifted chemical exchange (SCE), including, but not limited to, saturation transfer.

Continuous-wave (*cw*) saturation is in many ways the gold standard in CEST. The main advantages of a *cw*-presaturation are the spectral selectivity, the ease of simulation and data fitting, and its high efficiency in generating CEST contrast. *cw*-CEST experiments can be used for the determination of the single parameters affecting R_{ex}, namely k_b, f_b (the spin fraction) and R_{2b}. Modulating the amplitude ω_1 in CEST experiments can exploit the linear relations:

$$1/R_{ex}^{max} = \frac{k_b + R_{2b}}{f_b}\omega_1^{-2} + \frac{1}{f_b k_b}$$

$$0.25\Gamma = \frac{k_b + R_{2b}}{k_b}\omega_1^2 + (k_b + R_{2b})^2$$

This technique of microscopical parameter determination is called QUantification of Exchange by Saturation Power (QUESP, (13)). Closely related to it is the Quantification of Exchange by Saturation Time (QUEST) (13).

Pulsed CEST, on the other hand, developed mostly in response to clinical hardware constraints (SAR and Duty Cycle restrictions). Shorter saturation pulses require an amplitude profile that optimizes its spectral selectivity. Contrast generation is less efficient than *cw*, especially at high exchange rates. Despite its disadvantages, there are some exchange conditions where pulsed-CEST is comparable to *cw*. If the spin exchange is slow enough (the residence time long enough), it is possible to cause all spins to rotate during a short pulse's irradiation. Because of this, the meaning of a flip angle value for the CEST pulse is restored (generally in CEST, a FA value is a mere measure of pulse amplitude and does not represent an actual rotation because of the undergoing exchange). Quite intuitively, and already applied in hyperCEST, inversion pulses have the highest saturation transfer yield. In publications this is referred to as chemical exchange rotation transfer (CERT)((14)-(16)), and the condition for its use is that the pulse time: $\tau_p < 1/(k_b + R_{2b})$.

Frequency labeled exchange (FLEX) (17) is a technique that investigates the shifted chemical exchange (SCE) system by varying the evolution time (in the order of ms) between two excitation pulses of opposite phase. The water signal intensity is plotted against the evolution time to produce a FID-like composite oscillation, which contains multiple exchange signatures. The exchange information, as well as the chemical shift information, can be extracted after Fourier transformation. The technique has been also used on paramagnetic systems (18) and clinically (19). The FLEX approach is fundamentally different from ST, and offers some interesting advantages.

Spin lock experiments are in many ways similar to ST in detecting exchanging spins. A spin lock experiment flips the water magnetization on the transverse plane, then selectively keeps it on that plane through a *cw* or pulsed B_1 field. As the shifted pool is not locked on the plane, the decrease in transverse magnetization is a function of the SCE. The theoretical equivalence of spin-lock and CEST experiments has been the focus of Zaiss et alii (20)(21). Experimentally, SL experiments have been reported to yield higher SNR than *cw*-CEST, but cannot be corrected for B_0 inhomogeneities with the same ease.

1.4 CEST contrast agents

See review by Terreno et al. (2010)(22).

Generating CEST contrast is limited by multiple factors, with SAR, spin concentration and exchange rates being the principal determinants of sensitivity. A CEST contrast agent needs to either reach sufficient concentration in the tissue of interest, have multiple exchanging protons, or have exchange rates fast enough to compensate its low spin concentration.

To reach high spin concentrations, several strategies are possible: the use of safe biological molecules (glucose (23) for uptake studies), drugs approved for use at high dosage (CT contrast agents for pH imaging (24)(25)), and targeting or drug-delivery strategies (liposomial CEST (26)).

A necessary condition for rapid (>10 kHz) exchange rates is to avoid the fast exchange limit. If the exchange is too fast relative to the difference in chemical shift with the water, the signals will coalesce and no CEST analysis will be possible. One way of circumventing this problem - increasing the B_0 field strength - however, causes the energy deposited by the saturation RF field to increase (27). Moreover, the optimal irradiation amplitude (labeling efficiency, α) is higher for faster exchange rates (11)(28), making high magnetic fields unattractive for rapidly exchanging CEST compounds. A second alternative is to increase the chemical shift through shifting agents.

Paramagnetic ions, such as lanthanides, can be inserted in a chelating cage and potentially lead to extremely high shifts in the chelator's spins. This class of paraCEST compounds (Section 1.8) commonly makes use of rapidly exchanging protons and can be used at field strenghts lower than 3T. The major limitation of these molecules is their toxicity - which depends mostly on the chelate stability - and their development. Some paraCEST agents have been adapted with relative ease from gadolinium-chelating relaxation enhancers. Their biodistribution and stability can also be inferred from their Gd counterparts with reasonable accuracy.

Other than lanthanides, transition metal ions such as Fe^{II}, Co^{II}, and Ni^{II} can be employed for paraCEST complexes (29). Iron in particular offers considerable advantages in terms of toxicity.

Additional strategies to obtain measurable CEST signal include hyperpolarization (hyperCEST) (30), where ^{129}Xe is hyperpolarized through optical pumping, thereby greatly increasing its spin population difference. The technique is a modification of the hyperpolarized noble gas experiments performed in the late 1990s (31). Compared to most hyperpolarization experiments (^{13}C-labeled DNP and PHIP), the inert Xenon relaxes slowly to thermal equilibrium, allowing for use within a longer time frame. The chemical shifting is achieved through steric inclusion of the Xenon in a cryptophane cage (32), whereas the exchange rates depend on the noble gas' kinetics in entering and exiting the molecular cage.

Biotechnological strategies, such as nanoparticles, dendrimers, and liposomes (33) can be used in conjunction with CEST. The term lipoCEST denotes a technique that goes beyond simple drug delivery strategies of liposomial CEST formulations (34). In this case, rate-limited water exchange between the inside and the outside of a liposome is the determining factor. Although not strictly a paraCEST technique, lipoCEST employs paramagnetic compounds to shift the internal water's resonant frequency. Changes in the exchange rates can be brought about by modifications of the liposomial membrane's fluidity and its surface area (35).

1.5 In vivo CEST

The factors affecting CEST in vivo are numerous and oftentimes difficult to isolate. The proton exchange is affected by pH because of acid- or base-catalysis (36). The rates of reaction are also temperature-dependent, as well as being affected by molecular diffusion in the biological medium. Additionally, the proton transfer is catalyzed by ions in solution, such as phosphate ions (37) commonly used for buffering. In diaCEST experiments (with limited chemical shifts), multiple endogenous contributions from APT, APEX and NOE, as well as fat saturation need to be considered (Figure 1.3). Lastly, the signal-diluting effects from macromolecular MT and saturation spillover need to be considered.

Corrections for the contributions of direct water saturation and macromolecular MT have been studied in detail. Unsurprisingly, given the theoretical framework, simple isolation of MT effects is not sufficient. To circumvent this problem, some figures - starting from Z values - have been proposed in *cw*-steady state driven CEST. Z values are acquired on- and off-resonance symmetrical to the water frequency. Assuming symmetrical MT effects, and being spillover inherently symmetric, the figure Φ_{asym} (38)(39):

$$\Phi_{asym} = \frac{Z^{off} - Z^{on}}{Z^{off}} = \frac{M_Z^{off} - M_Z^{on}}{M_Z^{off}}$$

is spillover corrected, with Z^{on} and Z^{off} being the values of the Z spectrum that are on-resonance to the CEST peak's Larmor frequency and off-resonance (symmetrical with respect to water) to it.

A second figure, Φ_{Rex} (40):

$$\Phi_{Rex} = \frac{1}{Z^{on}} - \frac{1}{Z^{ref}}$$

has been proposed as a spillover and MT independent figure (Section 1.7). In this case, the reference value Z^{ref} must be experimentally independent from NOE, CEST and asymmetric MT effects. In paraCEST, it usually coincides with Z^{off}. In APT diaCEST, Z^{off} coincides with the broad NOE signal, and cannot be used. A viable experimental alternative is to fit a two-pool (MT and water) system to the Z spectrum points furthest removed from the CEST peaks to determine a baseline Z^{ref} value.

1.6 pH imaging and Ratiometric analysis

The clinical interest in the characterization of cancer tissues is steadily increasing. MR imaging techniques provide useful tools to study solid tumors, with the investigation of tumor heterogeneity being the main objective. Molecular imaging techniques allow the analysis of what have been defined the "hallmarks of cancer"(41).

Among the hallmarks, deviations in energy metabolism are of considerable importance for allowing uncontrolled cell proliferation. The abnormal energy metabolism manifests itself in many ways. 1.) An increased uptake of glucose due to GLUT1 upregulation, which is the target of both FDG-PET and glucoCEST imaging modalities. 2.) The creation of neovasculature and the regions of hypoxia and normoxia that arise from an inhomogenoeus tumor perfusion. Also related to hypoxia is (3.) the shifting of tumor cell metabolism from oxidative respiration to glycolysis. This phenomenon, however, can also occur in the presence of oxygen, the reasons for which have not been completely elucidated yet.

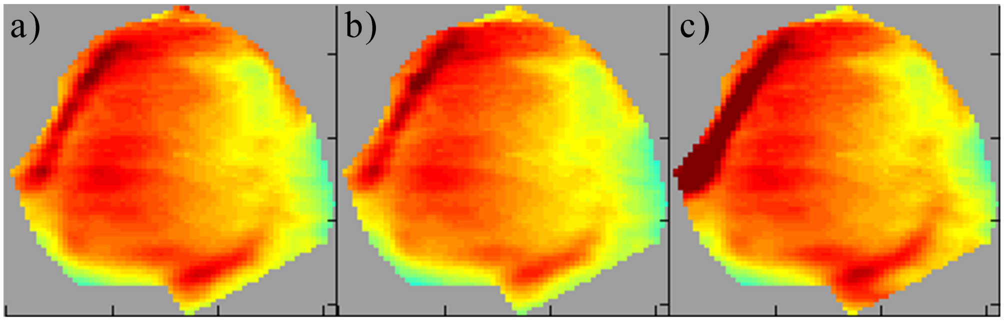

Figure 1.3: (a) APT, (b) APEX, and (c) NOE maps in an ROI from a coronal slice of a subcutaneous rat tumor. The values were calculated from the dataset presented in Figure 1.2, with a 6x3 cm half phase FOV, 128x64 acquisition matrix, interpolated to 256x128. The CEST analysis was performed yielding the Φ_{Rex} figure, with the baseline Z^{ref} value obtained through fitting as described in section 1.5. The color scales were normalized for comparison. The off-scale NOE signal is due to the direct saturation of fat (clearly detectable in the Z spectra). The similarities between the three maps point to the CEST experiment being more exchanging spin density than pH-weighted, because of the different pH catalysis the exchanging reactions would be subjected to.

An interesting feature in tumor heterogeneity is the presence of different populations of tumor cells, with differences in their energy-generation pathways. It has been reported (42), that symbiotically acting groups of cells complement their energetical needs by exchanging lactate. The first type of cells upregulate glucose uptake and anaerobic metabolism, secreting lactate which is taken up by better oxygenated cells for oxidative respiration. The increased production of lactate coincides with a lower pH of the intra- and extracellular matrix (43).

Pyruvate metabolism to lactate can be imaged by using hyperpolarized ^{13}C labeled pyruvic acid (44), whereas the pH of the tumor - intracellular or extracellular - can be assessed through various techniques. Hyperpolarized bicarbonate (45)(46) allows the pH to be measured through the relative intensities of the bicarbonate and carbon dioxide signals. The technique is ratiometric, and imaging is possible through CSI (chemical shift imaging) acquisition schemes, albeit with limited SNR. Other hyperpolarized compounds are suited for pH mapping, due to pH-induced chemical shifts of the ^{13}C-labeled moieties.

The analysis of phosphorous (^{31}P) chemical shifts represents the simplest way to measure pH (47). Due to the limited spin concentration and modest magnetogyric ratio, in vivo studies are limited to spectroscopy with long scan times. The ^{31}P

chemical species reporting on the pH are generally intracellular (48).

CEST offers unique advantages over other methodologies. While phosphorous pH is limited to MRS, and hyperpolarized ^{13}C very limited in resolution and by the T_1 decay time, CEST yields high resolution images and a much more practical measurement time window. On the other hand, the contribution of pH in the generation of CEST contrast is difficult to isolate, with ratiometric methods providing an elegant - albeit heavily signal-to-noise dependent - solution to the problem.

The magnitude of the chemical exchange can be greatly affected by pH, depending on the exchanging moiety. Being able to distinguish the pH contribution from the other factors affecting the CEST signal (spin concentration, temperature, spin diffusivity, presence of exchange-catalyzing ions), as well as correcting for competing and diluting effects (MT, spillover, T_1 and T_2) or instrumental inhomogeneities (B_1 and B_0 (49)), is a complex undertaking. One very elegant approach to pH determination is the ratiometric analysis, which requires multiple CEST proton pools on the contrast generating molecule.

Starting from the Bloch-McConnell description of M_z^a:

$$dM_z^a/dt = M_0^a R_1^a - \omega_2 M_x^a + \omega_1 M_y^a - (R_1^a + C_{ab})M_z^a + C_{ba}M_z^b$$

under the assumptions treated in (50) of complete saturation of pool b ($M_z^b = 0$) and negligible saturation of pool a ($\omega_1 M_x^a = \omega_2 M_y^a = 0$), the steady state magnetization is given by:

$$M_z^{a,ss} = M_0^a/(1 + C_a T_1^a)$$

where $C_a = k_a[Agent]$ and $[Agent]$ is the CEST pool's spin concentration.

Thus,

$$(M_0^a - M^{a,ss})/M^{a,ss} = k_a[Agent]T_1^a$$

Given the availability of two unrelated CEST pools, a concentration-independent figure can be determined:

$$ratio = \frac{k_b[Agent]T_1^a}{k_c[Agent]T_1^a} = k_b/k_c$$

The technique, presented by Ward and Balaban (51), allows the determination of pH with selected contrast agents. Other than multiple protons pools being a requirement, the pH catalysis of either exchange reaction needs to be different in order to reach sufficient pH sensitivity.

In conditions different from the ones stated (steady state, complete saturation of pool b and negligible saturation of pool a), the deviations from concentration

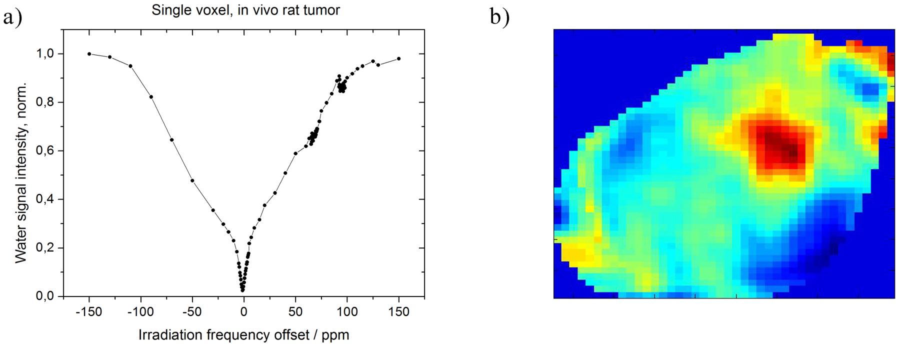

Figure 1.4: (a) Z spectrum of a MatBIII rat tumor from a single voxel acquired in vivo. The animal was injected SC with 0.2 ml of an unbuffered (pH 7.0), 1 M Yb-HPDO3A solution. The paraCEST compound is found in two slowly interchanging conformations, each giving rise to a CEST signal. The temperature-dependent chemical shifts of the proton pools are about 67 and 94 ppm at 37°C. By performing a ratiometric analysis using the Φ_{ratio} figure discussed in section 1.7, concentration-independent pH maps (b) can be obtained (self-normalized). To assign pH values to the images, a calibration curve mimicking the target tissue needs to be set up.

independence need to be considered. A more advanced ratiometric analysis starting from Φ_{Rex} is possible, and would be necessary if MT contributions are to be eliminated (Section 1.7, Figure 1.4).

A ratiometric treatment of the Φ_{Rex} is thought to be sufficiently accurate for paraCEST pH imaging in solid tumors. However, it would still assume constant temperature within the target tissue, as well as constant tissutal composition (spin diffusivity, exchange catalysis from tissutal components, such as phosphate ions).

1.7 The $R_{1\rho}$ formalism in CEST

See Zaiss and Bachert (2013)(7), Zaiss et al. (2014)(40).

Given the effective RF field in the rotating frame of reference

$$\boldsymbol{B_{eff}} = \boldsymbol{\omega_1}/\gamma + \boldsymbol{\Delta\omega}/\gamma$$

tilted from the z axis by the angle

$$\theta = tan^{-1}(\boldsymbol{\omega_1}/\boldsymbol{\Delta\omega})$$

the steady state Z value of the Z spectrum is:

$$Z(\Delta\omega) = \frac{M_Z(\Delta\omega)}{M_0} = cos^2\theta \frac{R_{1a}}{R_{1\rho}}$$

where $R_{1\rho}$ is the longitudinal relaxation rate of the water pool in the rotating frame, and is composed of an exchange-dependent component R_{ex} and a residual component R_{eff}:

$$R_{1\rho} = R_{eff} + R_{ex}$$

The residual component (the R_1 of water in the rotating frame) can be approximated to (78):

$$R_{eff} = R_{1a}cos^2\theta + R_{2a}sin^2\theta = R_{1a} + (R_{2a} - R_{1a})\frac{\omega_1^2}{\omega_1^2 + \Delta\omega^2}$$

and represents the origin of the spillover effect. On resonance, R_{ex} can be approximated to (7):

$$R_{ex} = C_b f_b \alpha$$

where C_b is the exchange rate of pool b, f_b its molar fraction, and α the approximated labeling efficiency:

$$\alpha = \frac{\omega_1^2}{\omega_1^2 + C_b(C_b + R_{2b})}$$

The previously mentioned figures Φ_{asym} and Φ_{Rex} can thus be explicited as:

$$\Phi_{asym} = \frac{R_{ex}}{R_{eff} + R_{ex}}$$

$$\Phi_{Rex} = \frac{R_{ex}}{cos^2\theta \cdot R_{1a}}$$

For ratiometric purposes, the ratio of $\Phi_{ratio} = \Phi^b_{Rex}/\Phi^c_{Rex}$ would be approximately T_1, B_1 and concentration independent, the molar fractions being constant.

$$\Phi_{ratio} \approx \frac{C_b f_b \alpha_b}{C_c f_c \alpha_c}$$

The evolution of this figure with pH would constitute the ratiometric calibration curve. For systems with multiple paraCEST pools, the different labeling factors and their dependence on ω_1, the chemical shift, and the exchange rates can be exploited to optimize the pH sensitivity (Chapter 3).

1.8 ParaCEST contrast agents

See review by Clore and Iwahara (2009)(53), also see Funk et al. (2013)(52).

Paramagnetic materials possess the property of increasing the density of the magnetic field lines of force passing through them (positive magnetic susceptibility). In most cases, if you exclude orbital paramagnetism, this is due to the presence of unpaired electrons in the molecule or atom. Spin paramagnetism is stronger than diamagnetism, so that in a molecule with unpaired electrons, the paramagnetic contributions trump the diamagnetic ones.

Paramagnetic ions have found use in NMR and MRI for structure determination purposes and for contrast generation respectively. There are three observables that can be exploited in NMR of paramagnetic systems: paramagnetic relaxation enhancement (PRE), pseudocontact shifts (PCSs) and residual dipolar couplings (RDCs). The last two can only be observed in systems with an anisotropic electron g-factor (i.e. where the electron possesses both spin and orbital angular momentum). PRE affects both longitudinal and transverse relaxation rates, with strong μ_{eff} (effective magnetic moment) and B_0 field dependencies. The relation stems from the Curie term relative to the dipole-dipole interaction between the nucleus and the time-averaged magnetization of the electrons. The Solomon-Bloembergen-Curie equations may take the form (with $T_{1e} << \tau_r$):

$$R_1 = \frac{2}{15}(\frac{\mu_0}{4\pi})^2 \frac{\gamma_N^2 g_{Ln}^2 \mu_B^2 J(J+1)}{r^6}[3\frac{T_{1e}}{1+\omega_N^2 T_{1e}^2} + 7\frac{T_{1e}}{1+\omega_e^2 T_{1e}^2}] + \frac{2}{5}(\frac{\mu_0}{4\pi})^2 \frac{\omega_N^2 \mu_{eff}^4}{(3k_B T)^2 r^6}[3\frac{\tau_r}{1+\omega_e^2 T_{1e}^2}]$$

$$R_2 = \frac{2}{15}(\frac{\mu_0}{4\pi})^2 \frac{\gamma_N^2 g_{Ln}^2 \mu_B^2 J(J+1)}{r^6}[2T_{1e} + \frac{3}{2}\frac{T_{1e}}{1+\omega_N^2 T_{1e}^2} + \frac{13}{2}\frac{T_{1e}}{1+\omega_e^2 T_{1e}^2}] + \frac{2}{5}(\frac{\mu_0}{4\pi})^2 \frac{\omega_N^2 \mu_{eff}^4}{(3k_B T)^2 r^6}[2\tau_r + \frac{3}{2}\frac{\tau_r}{1+\omega_e^2 T_{1e}^2}]$$

Where μ_0 is the vacuum permeability, γ_N the magnetogyric ratio of the involved nucleus, g_{Ln} the Landè factor of the lanthanide ion and J its total electronic angular momentum. μ_B is the Bohr magneton, r the distance between the nucleus and the electron. T_{1e} is the longitudinal relaxation time of the electron spin, ω_N and ω_e are the nuclear and electron Larmor frequencies. μ_{eff} is the effective magnetic moment of the Ln^{3+} ion, k_B the Boltzmann constant and τ_r the rotational correlation time.

The PRE interactions manifest themselves over relatively long distances (up to 35 angstrom). Because of the r^6 term in the SBC equations, PREs are perfectly suited for studying distance-dependent structural features of proteins. In paraCEST, shorter T_1 and T_2 relaxation times are usually an unwanted effect, unless their variation can be used to determine a contrast agent's concentration quantitatively.

Pseudocontact shifts depend on the position of the nuclear spin relative to the metal ion. There is a r^{-3} dependency for the shift, with relevant distances for PCSs being up to around 40 angstrom. In paraCEST, small changes in the relative distance of a moiety bearing the exchanging proton result in considerable chemical shifting. The magnetic susceptibility tensor (χ, rank 2) describes the volume magnetic interaction of the two vectors (field and magnetization). The angles of the nuclear spin's spherical coordinates, with the origin being the metal ion and the principal axes of χ, are ϕ and θ.

$$\delta_{PCS} = \frac{1}{12\pi} r^{-3} \Delta\chi_{ax}(3cos^2\theta - 1) + \frac{3}{2}\Delta\chi_{rh} sin^2\theta cos2\phi$$

with the axial and rhombic components of χ being:

$$\Delta\chi_{ax} = \chi_{zz} - \frac{1}{2}(\chi_{xx} + \chi_{yy})$$

$$\Delta\chi_{rh} = \chi_{xx} - \chi_{yy}$$

The relationship between the electron g and χ tensors is described by:

$$\chi_{kk} = \frac{\mu_0 N_A \mu_B^2 S(S+1)}{3k_B T} g_{kk}^2$$

where N_A is Avogadro's number and S the spin quantum number.

If molecules have no preference in orientation, tumbling samples an isotropic distribution, and dipolar couplings average to zero. Residual dipolar couplings (RDCs) arise from the preferential partial alignment with the magnetic field of molecules containing a paramagnetic center with an anisotropic g-tensor. This effect is exploited for protein characterization, but is of no interest in paraCEST.

The presented description of paramagnetic agents underlines the increased complexity in defining optimal experimental conditions for paraCEST. Sensitivity and competing contributions are the major problems of contrast media in CEST imaging. Contrast agent concentrations in the tissues of interest are usually limited to the 1-5 mM range. Given a sufficiently high chemical shift and saturating RF field, this limitation can be overcome by exploiting rapid (>10kHz) exchange rates. This requires finding the optimal B_0 field strength and $\Delta\omega$ chemical shift to balance labeling efficiency and SAR constraints.

Chelates of paramagnetic ions with exchanging protons - paraCEST agents - can satisfy the chemical shift requirements for use at relatively low field (1 T) (Chapter 2). The presence of multiple and magnetically equivalent exchanging protons is one strategy of increasing the spin concentration. However, drug development is constrained by chelate stability (and toxicity), the geometric position of the exchanging protons relative to the paramagnetic ion (related to the chemical shift), the rates of the exchange and the pH catalysis thereof, as well as the choice of the ion (among lanthanides (54) and transition metals (29)).

ParaCEST agents will continue to be relevant in preclinical studies, including tumor characterization for personalized medicine. Clinically, specifically designed paraCEST complexes might find use at low field (up to 1.5T).

1.9 Preclinical applications

Preclinical applications are the best setting for CEST and related techniques based on chemical exchange. The widespread availability of high-field ($\geq$ 4.7 T) MRI scanners, RF power amplifiers that allow *cw*-irradiation even at high amplitudes, and the lack of strict SAR monitoring all contribute to the ease of performing CEST experiments.

In diaCEST, the frequency separation at high-field results in the possibility of resolving single CEST peaks in the Z spectrum. This can lead to a higher number of metabolites and chemically exchanging molecules being detected. Among the endogenous signals, glycogen concentration in the liver has been investigated through CEST (GlycoCEST (55)) and cross-validated with ^{13}C MRS, with the goal of monitoring glycogen metabolism in diabetes and related pathologies. The creatine (CrEST (56)) CEST signal provides a marker for myocardial function, with good correlation to existing spectroscopical techniques ex-vivo.

Contrast agent based CEST has been mostly investigated in the preclinical setting. GlucoCEST (23) makes use of a concentrated glucose bolus (140 mM, 0.2 ml) at 9.4 T to assess glucose uptake in the tumor. The study performed a cross-validation of the results with FDG-PET.

ParaCEST agents have been proposed for pH-weighted and pH imaging in vivo (57)(58)(54), using the ratiometric method previously discussed. This is commonly done at high field (7 T) with Yb complexes while employing high amplitude *cw*-saturation (> 15 μT) unsuited for human use. This methodology is discussed in depth in chapters 2 to 4.

The ratiometric analysis for pH mapping in CEST has also been explored for diamagnetic molecules (diaCEST). CT contrast agents used in the clinical practice have been proposed as CEST agents because of their low toxicity, high allowed dosage and the presence of multiple exchanging protons. Iopamidol, Iopramide, and Iobitridol have undergone research for their pH mapping potential (24)(25)(59).

LipoCEST applications need to be distinguished in two modalities. Liposomes can be used as drug delivery systems that encapsulate a CEST contrast agent (26) for pH-weighted imaging (60) or liposome accumulation monitoring (61). The liposomial nanosystems can also be used in conjunction with a shifting agent to exploit the exchange between the inside and the outside water pools (62)(63). In the latter case, the rate of water exchange represents the determining factor for the CEST signal. The chemical shift of the encapsulated paramagnetic solution's spins is smaller than what is common for paraCEST agents, and the inhomogeneous distribution of paramagnetic ions causes unwanted, and B_0-dependent shortening of T_1 and T_2.

Despite the increased complexity of these systems, the potential of exploiting liposomial drug delivery strategies makes lipoCEST an interesting topic of research. A more exhaustive discussion on the conflicting mechanisms of lipoCEST can be found in chapter 4.

1.10 Clinical applications

See review by Kogan et al. (2013)(64).

CEST sensitivity is limited on clinical scanners, where SAR and RF duty cycle are restricted. Therefore, endogenous molecules present in the tissues at considerable concentrations have been the preferential target for CEST. To the author's knowledge, the only CEST contrast agent to have been tested in humans is Iopamidol (65). The region of interest in this case was the bladder, where the agent accumulates to high concentrations (tens of mM).

Among the endogenous CEST targets are glutamate (gluCEST (66)), glycosaminoglycan (gagCEST (67)), myo-inositol (MICEST (68)), and creatine (CrCEST or CrEST (69)). In addition, the heterogeneous amide proton pool can be investigated in amide proton transfer (APT) experiments. APT experiments generally assign the changes in CEST contrast to variations in tissue composition and pH, being aspecific both in terms of the molecules they target and the predominant source of ST (variations of exchange rate or spin concentration). However, specificity is not necessarily a prerequisite, and APT imaging has proven helpful in clinical tumor imaging (70)(71). The conclusions that can be drawn from APT imaging (as well as from APEX and NOE imaging) are mainly related to exchanging spin density. As such, the density of cells can be investigated and tumor tissue distinguished from oedema and necrosis.

Composite ST signal can be detected analogously in APEX (amine proton exchange) experiments. It should be noted that the assignment of the endogenous CEST signal to single molecules is not necessarily unequivocal. A single metabolite study might require prior knowledge of the tissue's composition, and oftentimes assume the CEST contribution being solely or predominantly attributable to the metabolite.

Other practical limitations include: 1.) length of the acquisition and susceptibility to movement artifacts, 2.) B_0-dependent frequency resolution, 3.) B_0-dependent SAR limitations, and (4.) extraction and quantification of the CEST signal from the background. Endogenous CEST will increase in relevance at fields higher than 3 T, depending on the optimum between saturation amplitudes (related to the exchange rates) and frequency resolution. Even at 3T, CEST has shown to yield clinically useful results, as well as being easily implementable.

To avoid the complexity of an accurate CEST analysis - and the accompaning error propagation - simple MTR_{asym} studies are commonly performed. Another pathway of CEST signal determination employs the difference to a fitted baseline. Either have been performed in a variety of clinical studies ((72)-(76)). While the declared target is usually APT protons, NOE (and, to some extent, MT) effects also contribute to the MTR_{asym} figure in the same offset range, and are therefore included in the analysis. If not corrected for, T_1 and B_1 inhomogeneities also play a role. An accurate APT analysis would require the possibility to resolve the APT peak in the Z spectrum, thus defining its baseline. Most clinical studies have been performed at a field strength of 3 T, insufficient for an accurate diaCEST peak resolution. Paech, Zaiss et al. achieved more accurate NOE MTR_{asym} results at 7T (77).

As the CEST effect has multiple dependencies, but a low sensitivity, extracting single parameter (pH, temperature, tissutal composition) information is very ambitious. APT mapping allows a more generalized approach to CEST, which is the reason why it has been the most sought after contrast source. The signal strength is generally higher than for APEX and it is not influenced by fat saturation like the NOE signal. It should not surprise that the medical requirement is one of simplicity and robustness, and while the use of contrast media for pH determination will remain an interesting topic for future research, pH-weighted and cell density CEST imaging are much closer to clinical applicability.

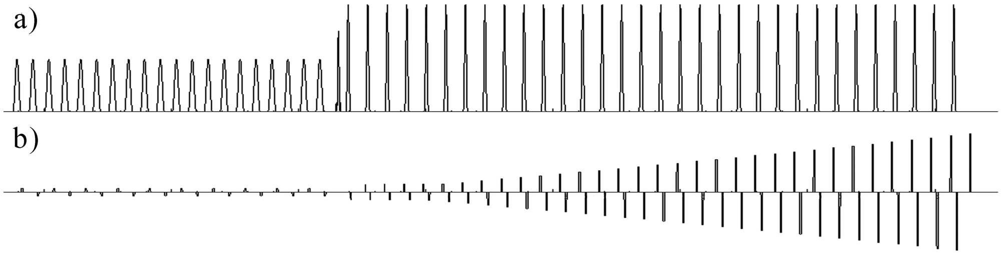

Figure 1.5: (a) Graphic view of a gaussian pulse train presaturation followed by a common RARE readout. The phase encoding gradients (b) underline the centric cartesian trajectory that was chosen for this sequence. After the saturation pulses, spoiler gradients of alternate polarity are played out (79).

1.11 MRI sequences for CEST

There are two main cathegories of CEST sequences. A single presaturation event can be used to reach a ST steady state, and after a spoiler gradient the resulting magnetization is acquired with common readout strategies. Alternatively, the saturation pulses can be interleaved in the acquisition scheme - effectively saturating offresonance before each excitation pulse - with the steady state being reached at some point during the acquisition.

The main advantage of the first approach is its simplicity. A presaturation pulse (or a train of pulses) precedes a standard MRI sequence. If available, existing MT sequences can be readily adapted. A sufficiently long presaturation guarantees an acquisition at the steady state. The readout is usually performed with a centric encoding in spin echo experiments (RARE, TSE, SSTSE ...). Alternatively, fast acquisition schemes such as EPI may also be used.

The advantage of an interleaved saturation is the possibility of imaging multiple slices faster (80). What effectively is a train of saturation pulses is applied between excitation-acquisitions, losing the flexibility of the presaturation pulse train in optimizing saturation and mixing (interpulse delay) times. In addition, a too long delay between the pulses will decrease the steady state level of the ST, because of relaxation. The steady state can be reached before the centre of the k-space through a composition of dummy scans and linear (or anti-centric) encoding schemes.

Interleaved saturation obviously doesn't allow *cw*-irradiation, which is an easy and very efficient way to generate CEST constrast in the preclinical setting (assuming the absence of SAR and DC limitations).

In pulse trains, the choice of the pulse shape, length, amplitude and interpulse delay depend on the CEST system. Gaussian pulses are a common choice for their high spectral selectivity at short pulse lengths, which makes them very versatile. Slowly exchanging systems can benefit from the CERT rotation regime mentioned previously. Fast exchanging systems, on the other hand, require high amplitude pulses, so that an RF pulse with a quickly rising amplitude profile would be more suited (e.g. Fermi pulses). Outside of the rotation regime, a longer RF duty cycle is normally advantageous.

Chapter 2

MRI CEST at 1T with large μ_{eff} Ln^{3+} complexes. Tm^{3+}-HPDO3A: an efficient MRI pH reporter.

Magnetic Resonance in Medicine 00:00–00 (2015)

MRI CEST at 1T With Large μ_{eff} Ln^{3+} Complexes T m^{3+}-HPDO3A: An Efficient MRI pH Reporter

Giaime Rancan,[2] Daniela Delli Castelli,[1] and Silvio Aime[1]*

Purpose: Chemical exchange saturation transfer (CEST) sensitivity relies on the prototropic exchange rate k_{ex} between the agent and the "bulk" water protons. To exploit large k_{ex}, a large frequency separation ($\Delta\omega$) between the pools of exchanging protons is necessary. For this reason, high magnetic fields are preferred. Herein it is shown that the use of paramagnetic CEST agents based on lanthanide (III) ions with large effective magnetic moments allows the carrying out of CEST experiments at the relatively low field strength of 1 tesla (T).

Methods: Measurements were performed on a 1T MR-scanner using continuous wave (cw)-presaturation with a spin echo sequence. ParaCEST complexes have been synthetized by mixing the ligand and Ln(III)Cl_3 in a stoichiometric ratio at room temperature and pH 7.

Results: Different lanthanide chelates were investigated (Tm-, Dy-, Yb-, Eu-HPDO3A, and Eu-DOTAMGly). Ratiometric (Tm-HPDO3A) and selective detection (Eu-DOTAMGly and Tm-HPDO3A) experiments have been proven feasible in vivo.

Conclusion: In vitro experiments demonstrated the feasibility of the CEST methodology at 1T for nearly every paraCEST candidate under investigation, except for Eu-HPDO3A. Among the studied compounds, Tm-HPDO3A proved suitable for the application of a ratiometric method for assessing pH both in vitro and in vivo. **Magn Reson Med 000:000–000, 2015. © 2015 Wiley Periodicals, Inc.**

Key words: CEST; HPDO3A; low-field CEST; paraCEST; pH mapping

INTRODUCTION

Chemical exchange saturation transfer (CEST) (1) contrast agents act by transferring saturated magnetization to the bulk water via proton exchange (2–5). The contrast generation is selective, occurring when a small bandwidth saturating radio frequency (RF) field is centered at the exchanging spins' resonant frequency. The rate of the proton exchange is affected by many physicochemical parameters, the information of which can be encoded with CEST. This allows a variety of experiments to be performed that would be impossible with conventional relaxation enhancer agents (6,7).

To avoid the fast exchange limit (and signal coalescence), a frequency separation higher than the exchange rate is necessary in CEST experiments ($\Delta\omega >> k_{ex}$). For this reason, field strengths higher than 3 tesla (T) are commonly employed to resolve saturation transfer (ST) signals. However, rapid (10 kHz) exchange is advantageous if the exchanging spins' concentration in the tissue of interest is low. Factors affecting spin concentration include the agent's biodistribution and the number of magnetically equivalent exchanging spins on each molecule. In addition to high frequency separations, rapid exchange also requires high RF amplitudes to express its full ST potential. As the specific absorption rate (SAR) increases with B_0 (8), finding the optimal magnetic field is essential for CEST.

An appealing class of CEST agents are the paraCEST chelates, which make use of paramagnetic ions to achieve large chemical shifts (> 30 parts per million (ppm)). The main determinants of the induced shift are the paramagnetic ion (9) and the exchanging proton's distance and angle relative to the main magnetic axis (10,11) in the ligand. The HPDO3A ligand (Fig.1, left) is of high interest for the clinical translation of paraCEST. Its Gd complex is one of the safest and most stable MRI relaxation enhancers used in clinical practice (12,13). Gd-HPDO3A (Prohance, Bracco Imaging, Milan, Italy) distributes in the vascular and extravascular compartments, is quickly excreted though the kidneys, and displays an extremely favorable toxicity profile. For use in CEST, lanthanide analogues of Prohance (Bracco Imaging) benefit from the high chemical shifts of the coordinating hydroxyl moiety and its proton's rapid exchange with water. Because the exchange is base-catalyzed, these molecules can also act as reporters of pH, a highly interesting biomarker. Furthermore, for selected HPDO3A chelates, it is possible to avoid the need for concentration determination when quantifying pH. These chelates are found in different isomeric forms with defined ratios, of which the CEST signals may be resolved in a Z spectrum. A ratio of the CEST effect from the two proton pools can be used to set up calibration curves. The slope of the curve, the pH sensitivity, is dependent on the difference in pH catalysis for the two pools.

Yb-HPDO3A has been proposed as an efficient agent for pH mapping at high field (7T) (14), with SAR limitations being the main translational issue. The chelate is found in two diastereomeric forms, square antiprismatic (SAP) and twisted SAP (TSAP) (15), which allow the use of the ratiometric method. Additionally, the pH sensitivity for this compound is optimal in the physiological range.

---

[1] University of Turin, Molecular Imaging Center, Torino, Italy.

[2] Technical University Munich, Klinikum rechts der Isar, München, Germany.

Grant sponsor: The project was supported by the Technische Universität München–Institute for Advanced Study, funded by the German Excellence Initiative.

*Correspondence to: Prof. Silvio Aime, University of Turin, Molecular Imaging Center, via Nizza 52, Torino, IT, 10125. E-mail: silvio.aime@unito.it.

Received 29 July 2014; revised 24 November 2014; accepted 29 November 2014

DOI 10.1002/mrm.25589

Published online 00 Month 2015 in Wiley Online Library (wileyonlinelibrary.com).

© 2015 Wiley Periodicals, Inc.

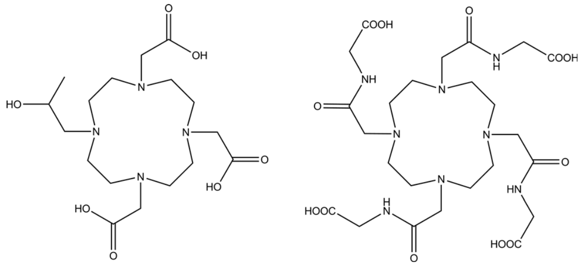

FIG. 1. Chemical structure of the HPDO3A (left) and DOTAMGly (right) ligands.

Other lanthanide ions endowed with large effective magnetic moments (μ_{eff}) have not been considered for fields higher than 3T because of their unfavorable, B_0-dependent, longitudinal relaxation properties. In this work, a screening of HPDO3A chelates was performed at 1T. The europium chelate of DOTAMGly (Fig. 1, right) was also included because the water molecule directly coordinated to its lanthanide ion is highly shifted but has a long enough residence time on the complex to avoid the fast exchange limit. It is demonstrated how CEST hallmark experiments – the ratiometric method and the selective irradiation of different CEST agents – are feasible at 1T. In addition, the relevant advantages of paraCEST at low fields are discussed.

THEORY

Relaxation in solutions containing paramagnetic complexes has been the subject of extensive investigation (16–18). Its relevance to the design and selection of paraCEST contrast agents is paramount, particularly in relation to the chemical shift of the exchanging protons and T_1 effects on the bulk water. Contributions to proton spin longitudinal relaxation are dependent on the electronic longitudinal relaxation (T_{1e}) involved in the electron–proton coupling as well as on rotational effects. The relevant Solomon-Morgan-Bloembergen equation takes the form:

$$R_1 = \frac{2}{15}\left(\frac{\mu_0}{4\pi}\right)^2 \frac{\gamma_N^2 g_{Ln}^2 \mu_B^2 J(J+1)}{r^6}\left[3\frac{T_{1e}}{1+\omega_N^2 T_{1e}^2}+7\frac{T_{1e}}{1+\omega_e^2 T_{1e}^2}\right] + \frac{2}{5}\left(\frac{\mu_0}{4\pi}\right)^2 \frac{\omega_N^2 \mu_{eff}^4}{(3k_B T)^2 r^6}\left[3\frac{\tau_r}{1+\omega_N^2 \tau_r^2}\right] \qquad [1]$$

where γ_N is the magnetogyric ratio of the considered nucleus and ω_N its Larmor frequency. ω_e is the electron spin precession frequency. g_{Ln} is the Landé factor of the considered lanthanide ion, μ_{eff} its effective magnetic moment, and J its ground state value. μ_B is the Bohr magneton, μ_0 the vacuum permeability, and k_B the Boltzmann constant. T is the absolute temperature, r the electron-nuclear distance, and τ_r the rotational correlation time.

Particularly relevant for the choice of lanthanide ions are their values of μ_{eff} and J (Table 1). The second term of Eq. [1] –the Curie relaxation term – results from the rotational changes in the interaction of the nucleus with the magnetic dipole moment. Especially at higher fields, the Curie term's dependency on $\mu_{eff}{}^4$ becomes an important factor for spin relaxation. Other general considerations on field strength and temperature effects on T_1 can be made based on Eq. [1], although temperature-dependent changes in viscosity of biological matrixes, and thus rotational correlation times, are nontrivial. Values of T_{1e} for the considered lanthanides are in the order of 10^{-13} s, just above the solvent-complex collision boundary (19). Because $\tau_r >> T_{1e}$ for the studied ions, the first term of Eq. [1] only contains T_{1e}. An exhaustive description of the subject has been given by Funk and Fries (20).

Faster longitudinal relaxation at high magnetic fields is disadvantageous for paraCEST. Lanthanides with higher μ_{eff} are especially affected by high fields, precluding many possibilities for contrast agent selection. Conversely, at moderate field strengths, the host of suitable lanthanides is extended, as is exemplified by the agent Tm-HPDO3A.

The effect of temperature in paraCEST is more complex, involving chemical shift, exchange rates, viscosity, and rotational correlation times—as well as affecting T_1 through the Curie term. It is therefore apparent that a careful determination of ratiometric calibration curves is necessary to achieve meaningful pH weighting—or for simple aqueous solutions, accurate pH determination.

CEST ratiometric analyses are based on the relationship presented in Ward's seminal work (21):

$${}^{M_s}\!\big/_{M_0} \approx \frac{1}{1+k_{ex}\cdot[spin]\cdot T_{1w}} \qquad [2]$$

Where M_s is the magnitude of the saturated water pool, M_0 of the unsaturated or control saturated magnetization, T_{1w} the T_1 of bulk water, (spin) the spin concentration in the sample, and k_{ex} the exchange rate relative to the observed spin.

By defining the ST efficiency as $(M_0\text{-}M_s)/M_0$, a concentration independent figure of merit is:

$$ratio = \frac{ST_{SAP}(1-ST_{TSAP})}{ST_{TSAP}(1-ST_{SAP})}$$

The "ratio" is solely dependent on the relative changes in exchange rates due to pH catalysis but is independent of T_{1w} and the contrast agent's concentration. As is true for Eq. [2], this condition holds for steady-state saturation or small changes in concentration (< 10 mM).

METHODS

The HPDO3A ligand was kindly gifted by Bracco Imaging S.p.A. The Dy^{3+}, Yb^{3+}, and Tm^{3+} complexes were prepared and characterized according to the published methods. Eu-DOTAMGly has been synthetized, as reported previously. CEST MRI experiments were performed at 1T on a Bruker Icon spectrometer running Paravision 5.1 (Brucker, Billerica, MA). For in vitro experiments, temperature control was achieved by circulating heated water around the phantom. A rapid acquisition with relaxation enhancement (RARE) spin-echo sequence (rare factor 32) with an echo time of 6 ms and

Table 1
Solution T_1 values of the studied chelates (30mM) at different B_0 and their effective magnetic moment (μ_{eff}) and ground state J values.

Ln^{3+}-HPDO3A (30 mM)	T_1 (1T) (ms)	T_1 (3T) (ms)	T_1 (7T) (ms)	μ_{eff}	J
TmHPDO3A	378	266	210	7.6	6
YbHPDO3A	935	827	762	4.5	7/2
DyHPDO3A	157	114	100	10.6	15/2
EuDOTAMGly	1495	1360	1286	3.4	0

repetition time (TR) of 7,000 ms was used (centric encoding; isotropic field of view (FOV) 55 mm; acquisition matrix 32 × 32; 3-mm slice thickness (rats); 4 averages, or isotropic FOV 60 mm; 64 × 64, 2-mm slice thickness (mice)). For in vivo acquisitions, the TR was set to 5,000 ms. Unless otherwise specified, the imaging sequence was preceded by a saturation scheme consisting of a rectangular pulse (1,500 ms) with RF amplitude of 24 μT. Z spectra acquisition in the bladder was performed through alternate sampling of 79 frequencies in the range between ± 207.6 ppm. In vivo per-pixel and region-of-interest (ROI) analyses were performed using custom-written MATLAB scripts (MathWorks, MA). Data analysis included a B_0-correction routine employing cubic spline interpolation of the Z spectra. Voxels not satisfying the quantification requirements (9σ) are filtered from the image. T_1 measurements were performed on a Bruker Avance 300 (7T), on a Bruker Biospec 3T, and on a Bruker Icon 1T scanner, by using standard saturation recovery sequences. Reported ratios of SAP/TSAP isomers were determined by high-field spectroscopy (14T) under negligible-exchange conditions (pH 4.0, 25°C); isomer assignment was performed as reported (15). Phantom pH values in the range of temperatures considered did not deviate substantially.

Simulations were performed using the numerical exponential solution (22) to the Bloch equations modified for three-pool exchange (23) and were additionally used to assess single parameter dependency of the ST signal. Fittings to the model were performed through Z spectra on the 34°C dataset. The saturation protocol for this study was chosen experimentally based on in vitro measurements. Among the best performing saturations, a compromise between saturation efficiency, instantaneous SAR, and in vivo saturation spillover was sought.

Approval for the use of test animals for imaging was granted by the competent authorities.

RESULTS

Z-spectra of the buffered aqueous solutions (30 mM, pH 7.4, 25°C) of Dy-, Tm-, and Yb-HPDO3A at 1T are reported in Figure 2. High-resolution NMR spectra acquired at 14T showed that the three HPDO3A complexes investigated are present in solution as SAP and TSAP isomers: Dy-HPDO3A 0.88/0.12 (molar ratio SAP/TSAP); Tm-HPDO3A 0.80/0.20; and Yb-HPDO3A 0.67/0.33. Dy^{3+} and Yb^{3+} complexes display only one peak in the Z spectrum at 1T. In the case of Dy-HPDO3A, the single CEST signal likely represents the dominant SAP isomer, whereas the second isomer could not be detected in the Z spectrum for sensitivity reasons. Yb-HPDO3A displays one broad peak at approximately 80 ppm as a result of the unselective irradiation of SAP and TSAP isomers. The signal coalescence at 1T is the main reason why the ST% from Yb-HPDO3A is more intense than the split signals obtained from the previously reported experiment carried out at 7T (14), with longer T_1 times being a secondary contribution. In the Z-spectrum of Tm-HPDO3A, both SAP and TSAP peaks are detected.

Due to the large paramagnetic induced shifts, all three complexes may act as CEST agents on an MRI scanner operating at 1T. The differences in intensities of the reported CEST response reflect the ability of each complex to transfer saturated magnetization under the given experimental conditions (B_0, B_1, temperature, concentration, and pH).

Theoretical steady-state saturation transfer efficiency is directly proportional to the T_1 of the bulk water resonance. It was experimentally confirmed that the T_1 of paramagnetic Ln^{3+}-containing solutions (where $Ln \neq Gd$) decreases with higher applied B_0 fields (Table 1) (Fig. 3, right). This contribution to ST accounts for the trends pictured in (Fig. 3, left), but becomes secondary to saturation spillover at small frequency offsets.

Inspection of the Z-spectrum of Tm-HPDO3A shows that the saturation transfer to the water resonance occurs when the irradiation offset is around 71 and 185 ppm. The two isomers are involved in a mutual exchange

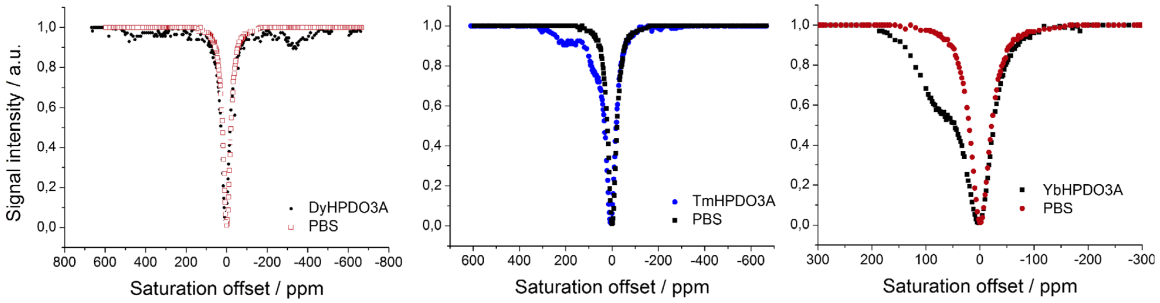

FIG. 2. Z-spectra of Dy-,Tm-, and Yb-HPDO3A 30 mM solutions recorded at 1T, pH 7.4, 25 °C, irradiation amplitude 24 μT, irradiation time 1 s, and the phosphate buffered solution standard. For Dy-HPDO3A, only the excess SAP isomer (76% diastereomeric excess) is detectable. Yb-HPDO3A displays a single signal in the Z spectrum from the two unresolved diastereomers.

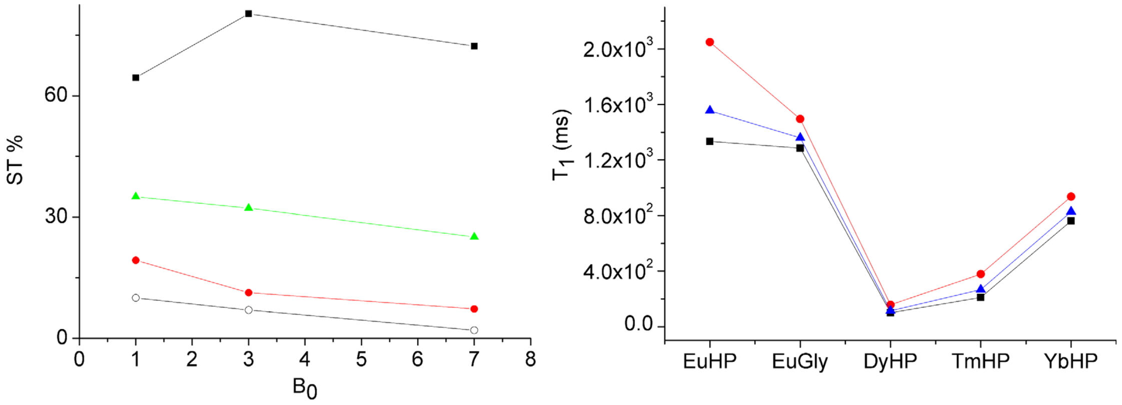

FIG. 3. (Left) ST% as a function of B_0 (T) for 30mM solutions of the following complexes measured at 20 °C: Yb- (green, triangle); Tm-SAP- (red, circle); and Dy-SAP-HPDO3A (open circle), as well as Eu-DOTAMGly (black, square). RF irradiation: 24 μT, 1 s. (Right) T_1 values of the solutions at 20 °C for the same complexes at the B_0 of 1T (red, circle), 3T (blue, triangle), and 7T (black, square).

process, which does not hamper their selective irradiation. The prototropic exchange between the hydroxyl moieties and water is base-catalyzed and increases with pH. Additionally, the structural differences between the two isomers result in considerably different prototropic exchange rates of the hydroxyl protons. This is well reflected in the diagram reported in Figure 4, where the ST% is plotted as a function of pH for the two isomeric forms.

This difference in the pH response of the ST effects is at the heart of the ratiometric analysis. An unequivocal assignment of pH can be performed through a concentration-independent calibration curve (Fig. 5). Because ST is also affected by temperature, multiple ratiometric curves are needed to accurately assign the pH, as well as the knowledge of the temperature of the target solution. The latter can be elegantly determined through the chemical shift of the contrast agent's signals, provided a fine enough frequency sampling of the Z spectrum is performed. To that end, ST measurements were carried out at three temperatures. An excellent agreement was found between the value calculated from the calibration curve (Δω against temperature) and the actual temperature measured with an ordinary thermometer.

Assessment of the method's concentration sensitivity, using sequence parameters matching the in vivo experiments, confirmed the higher ST effect at lower fields. At 1T, the in vitro limit of quantification (LOQ, 9σ) for ST% is 3.15% and 3.88% for the SAP and TSAP signals, respectively (pH 6.5, 25°C). The limits of quantification correspond to a local concentration between 10 and 15 mM (Fig. 6). The same measurements performed at 7T (data not shown) did not satisfy the quantification requirements, with a mere 2.4% and 3.0% ST effect at 30 mM, below the LOQ boundaries. This finding supports the previously indicated reasoning in favor of low

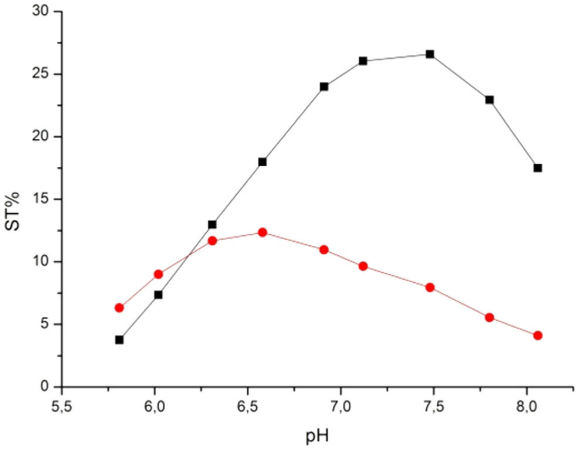

FIG. 4. ST% as a function of pH of the TSAP (red, circle) and SAP (black, square) hydroxyl protons of 30 mM Tm-HPDO3A solutions, 37 °C, 1T, obtained after a continuous wave irradiation of 24 μT, 1 s.

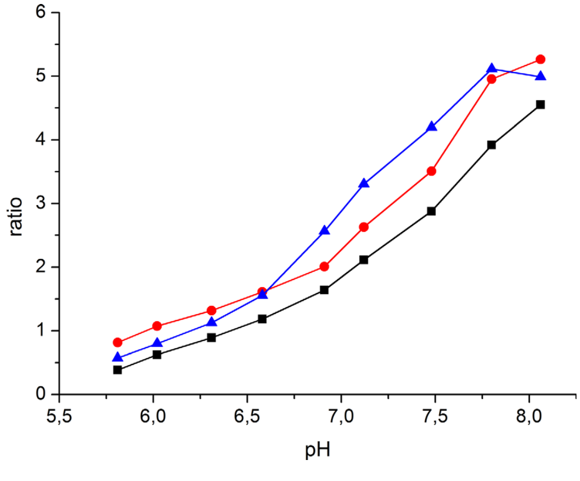

FIG. 5. Ratiometric plot from variable-pH, 30 mM Tm-HPDO3A solutions at 37 °C (red, circle), 34 °C (black, square), and 25 °C (blue, triangle), obtained after a continuous wave irradiation of 24 μT, 1.5 s.

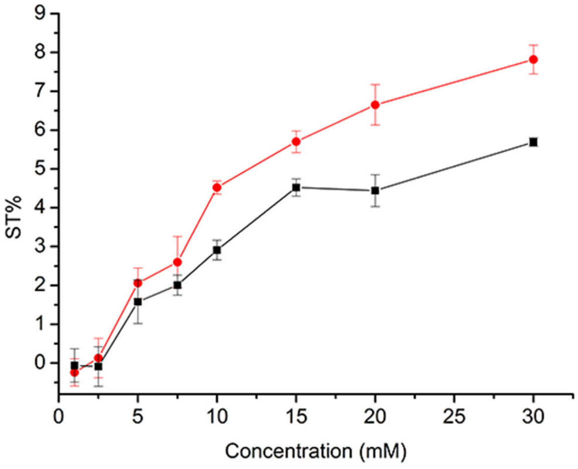

FIG. 6. ST% as a function of concentration for Tm-HPDO3A at 1T, pH 6.5, 25 °C of the TSAP (red, circle), and SAP (black, square) signals, with SD error bars from multiple acquisitions. Scans were performed with in vivo imaging parameters, and a continuous wave irradiation of 24 μT, 1.5s.

to moderate field strengths (< 1.5T) for paraCEST. Especially for complexes with high μ_{eff} lanthanide ions such as Tm^{3+}, their use as CEST contrast agents is only possible at these fields.

The promising Tm-HPDO3A was also tested in vivo as a pH reporter. In order to guarantee sufficiently high concentrations of the agent, the pH was mapped in the bladder and kidneys because – analogous to ProHance (Bracco Imaging)–these are the regions where the complex accumulates along its excretion pathway. Figure 7 and Supporting Figure S1 report the MR-CEST pH map obtained from a ROI of a rat's bladder 40 minutes after the intravenous administration of a bolus of Tm-HPDO3A (1.6 mmol/kg). From the $\Delta\omega$ value in the Z-spectrum, the temperature of urine in the bladder was 33°C. The pH value obtained in vivo, by using the calibration curve calculated at 34°C, was 7.3. The calculated pH only slightly deviates from the actual pH of the urine, measured by an ordinary pH-meter (7.2). The ratiometric analysis on the kidney region yielded pH values around 6.7 ± 0.2. Unfortunately, the voxel size (8.86 mm^3) used in this experiment does not allow discrimination between the different compartments of the organ.

Figure 8 shows the comparison between the Z-spectra acquired at 7T and 1T on a solution containing 20 mM of Eu-DOTAMGly at pH 7.4 and 20°C. The ST% of this solution is higher than that of the HPDO3A complexes discussed in this paper due to the combination of longer solution T_1 values, higher number of irradiated protons (2 protons belonging to the bound water molecule), and different exchange rates. It is worth noting that the ST efficiency for Eu-DOTAMGly does not increase upon lowering of the external field (Fig. 4), contrary to what occurs for the other complexes of this study. This is likely because the chemical shift of the mobile protons belonging to Eu-DOTAMGly is smaller than those belonging to the mobile pools of the Ln-HPDO3A (Ln = Yb, Dy, and Tm) complexes. The increase in saturation transfer from a longer T_1 is compensated by the loss of efficiency due to saturation spillover. In addition, the increase in T_1 of the Eu^{3+} complex is smaller than it is for lanthanides with higher μ_{eff} values. The separation between the hydroxyl proton resonance belonging to the TSAP isomer of Tm-HPDO3A (185 ppm) and the resonance of the bound water protons belonging to Eu-DOTAMGly (38 ppm) is large enough to detect these two contrast agents in the same solution. Figure 9 shows the ST maps of a mouse bladder acquired before and after the intravenous injections of a solution containing Tm-HPDO3A or Eu-DOTAMGly at the dose of 0.5 mmol/kg. After irradiating at 38 ppm, only the bladder of the mouse injected with Eu-DOTAMGly shows quantifiable ST. Conversely, only the bladder of the mouse injected with Tm-HPDO3A generates CEST contrast by irradiating at 150 ppm, demonstrating the feasibility of selective detection. When irradiating at 70 ppm, the selectivity is lost and both agents were detected.

DISCUSSION

The high chemical shifts of paraCEST contrast agents allow the exploitation of rapid proton exchanges at magnetic fields otherwise unsuitable for CEST experiments. Rapid exchanges and high amplitude saturation RF pulses are necessary to generate quantifiable ST contrast in paraCEST. Simulated SAR is reported to rise with the square of B_0 up to 100 MHz and then linearly up to 300 MHz (8). Therefore, provided that the frequency separation is sufficient, low field applications should be sought to minimize energy deposition. Moreover, for rapidly exchanging systems, short, high amplitude RF pulses are

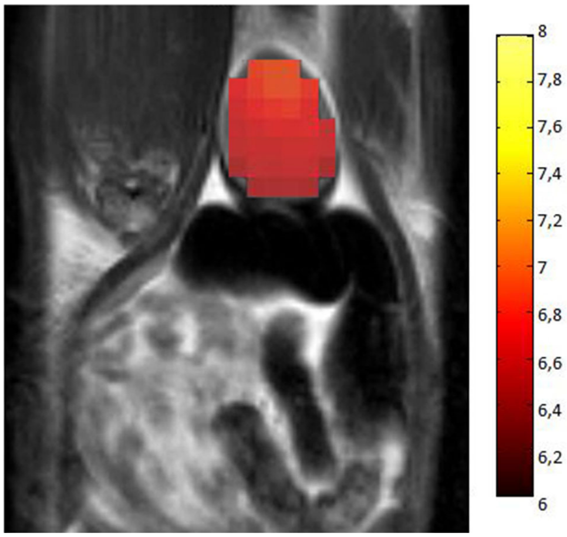

FIG. 7. CEST pH map in the ROI of a rat's bladder superimposed to an anatomical reference using Tm-HPDO3A as CEST agent at 1T, with a 32 × 32 matrix, FOV 55 mm, 3-mm slice, in a one-shot RARE acquisition preceded by a continuous wave irradiation (24 μT, 1.5 s). The homogeneous pH values from the ROI are in accordance with the measured pH of the urine.

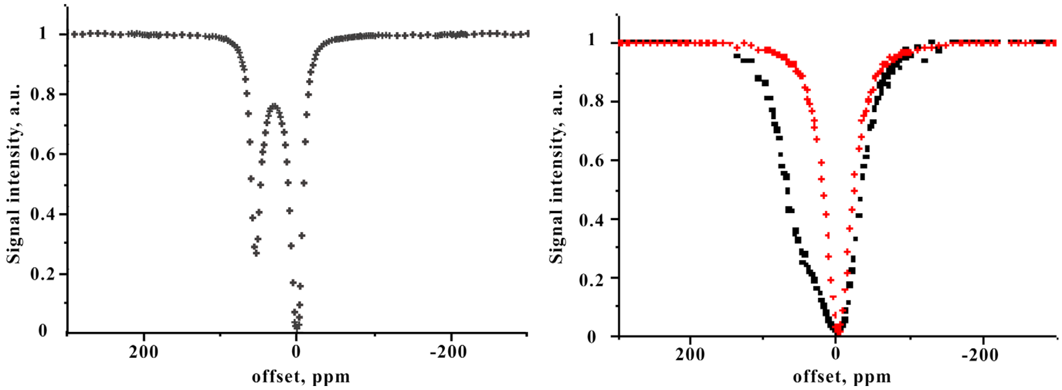

FIG. 8. Z spectrum of a 30 mM Eu-DOTAMGly solution buffered at pH 7.4 with B_0 of 7T (left) and 1T (right; red crosses are the phosphate buffered solution reference) at 20 °C, with a continuous wave irradiation of 24 μT, 1 s.

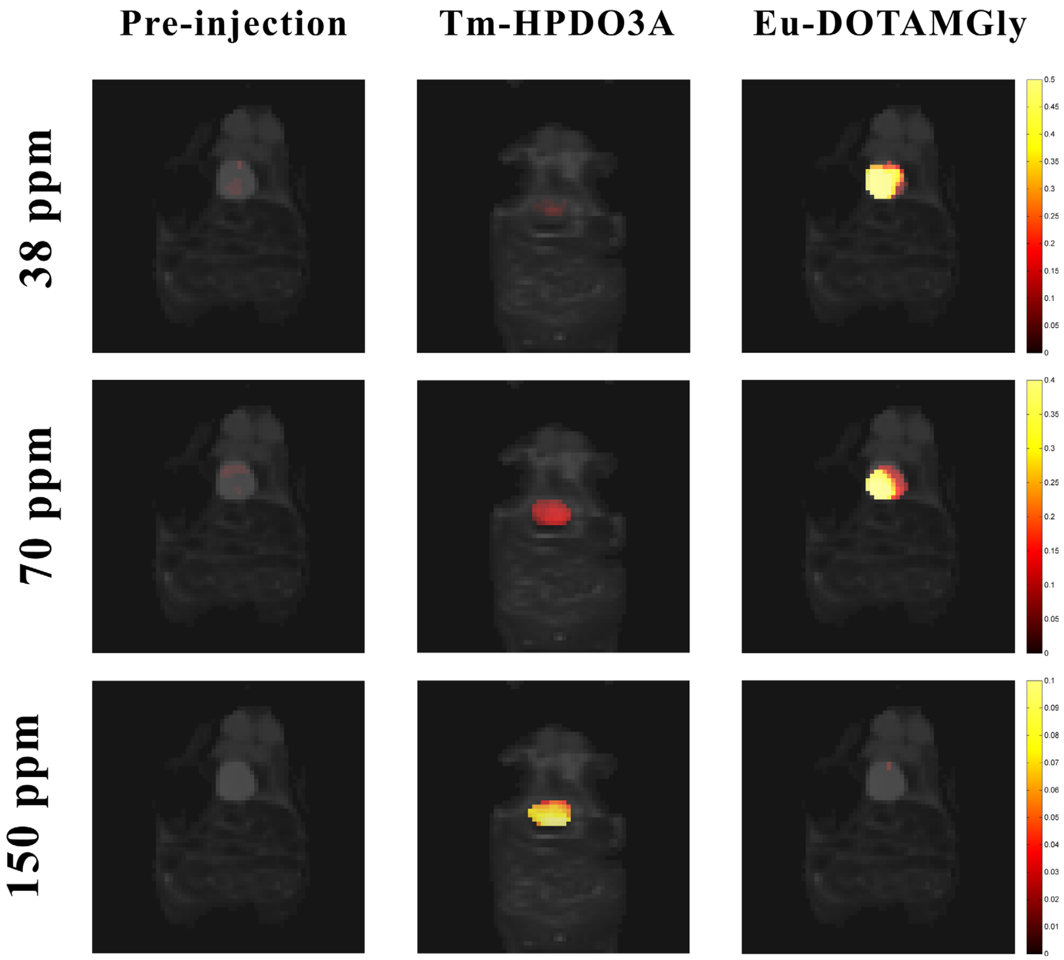
Pre-injection
Tm-HPDO3A
Eu-DOTAMGly
38 ppm
70 ppm
150 ppm
0.5
0.45
0.4
0.35
0.3
0.25
0.2
0.15
0.1
0.05
0
0.4
0.35
0.3
0.25
0.2
0.15
0.1
0.05
0
0.1
0.09
0.08
0.07
0.06
0.05
0.04
0.03
0.02
0.01
0

FIG. 9. ST map in the bladder at three offset frequencies: before injection, after intravenous administration of 0.5 mmol/kg Tm-HPDO3A, after intravenous administration of 0.5 mmol/kg Eu-DOTAMGly. CEST continuous wave irradiation was 24 μT, 1.5 s. The images show codetection at the offset value of 70 ppm, but independent contrast generation of the two agents at 38 and 150 ppm offsets.

preferred to longer irradiation at the same total energy. Additional signal can be obtained from the use of numerically optimized saturation pulses from which selective detection can also benefit by exploiting the difference in exchange rates between paraCEST chelates.

There are several other advantages for low-field paraCEST applications, the field-dependent T_1 effects of solutions containing paramagnetic ions being the most prominent. A reduction of T_{1w} from 378 to 210 ms results in a simulated signal loss of 40% for the SAP and of 37% for the TSAP isomers of Tm-HPDO3A, using the irradiation conditions stated previously. The smaller B_1^+ and B_0 inhomogeneities constitute a third advantage for CEST at lower magnetic fields. Ratiometric approaches employing different saturation pulses gain in relevance, and less frequency sampling is necessary for B_0 correction.

ParaCEST agents derived from relaxation enhancers offer clear advantages in terms of clinical translatability and availability. Prohance (Bracco Imaging) analogues possess high chelate stability and may present themselves in isomeric forms, allowing a ratiometric analysis to be performed. As previously stated, CEST optimality is heavily dependent on T_1 effects and the availability of multiple, rapidly exchanging, highly shifted protons. Optimal properties can be only achieved if the agents are designed and screened for use in CEST. For instance, water molecules directly coordinating the paramagnetic ion, unless used for a saturation transfer, are undesirable because of their T_1 relaxation contributions. The availability of multiple coordinating moieties with pH-catalyzed proton exchanges can also be the target of drug design.

The performed experiments confirm the possibility of detecting CEST signals in vivo at reasonable injection volumes and concentrations. The quantification of the signal is straightforward in anatomical regions where the contrast agent accumulates. For the present proof of concept, the determination of ratiometric calibration curves requires no particular considerations other than being performed at the relevant temperature. Should the anatomical target be different, for instance the extracellular matrix of a tumor, additional care should be put into calibration curve determination. Other factors would increase in relevance, such as the effect of the chemical environment (viscosity, proton diffusion) and of the T_2 relaxation on the ST response, the treatment of which is beyond the present work.

CONCLUSION

MR-CEST imaging can be carried out at 1T by exploiting paramagnetic molecules able to induce large $\Delta\omega$ with respect to the water proton resonance. A large $\Delta\omega$ allows for the exploitation of the high prototropic exchange rates, which are one of the main determinants of the efficacy of a CEST agent. Because fast exchange rates require high-saturation RF amplitudes to reach their full transfer potential, imaging at 1T has considerable advantages in terms of energy deposition. Paramagnetic complexes of ligands containing exchangeable protons in close proximity to a high μ_{eff} Lanthanide (III) ion, such as Dy^{3+}, Yb^{3+}, Eu^{3+}, and Tm^{3+}, appear to be good candidates for CEST applications at low to intermediate magnetic field strengths. ST efficiency increases at low field due to the longer T_1 of solutions containing lanthanides other than gadolinium. When two corelated pools of mobile protons are present, it is possible to design a ratiometric approach for concentration-independent pH assessment. In this regard, Tm-HPDO3A has shown to be a promising chelate for pH determination in vivo at 1T. The herein reported results have demonstrated that hallmark CEST experiments such as ratiometric pH mapping and selective excitation can be performed at 1T.

REFERENCES

1. Ward KM, Aletras AH, Balaban RS. A new class of contrast agents for MRI based on proton chemical exchange dependent saturation transfer (CEST). J Magn Reson 2000;143:79–87.
2. Woods M, Woessner DE, Sherry AD. Paramagnetic lanthanide complexes as PARACEST agents for medical imaging. Chem Soc Rev 2006;35:500–511.
3. van Zijl PCM, Yadav NN. Chemical exchange saturation transfer (CEST): what is in a name and what isn't? Magn Reson Med 2011;65: 927–948.
4. Terreno E, Castelli DD, Aime S. Encoding the frequency dependence in MRI contrast media: the emerging class of CEST agents. Contrast Media Mol Imaging 2010;5:78–98.
5. Sun PZ, Wang Y, Dai ZZ, Xiao G, Wu R. Quantitative chemical exchange saturation transfer (qCEST) MRI – RF spillover effect-corrected omega plot for simultaneous determination of labile proton fraction ratio and exchange rate. Contrast Media Mol Imaging 2014;9: 268–275.
6. Zhang S, Merritt M, Woessner DE, Lenkinski RE, Sherry AD. PARACEST agents: modulating MRI contrast via water proton exchange. Acc Chem Res 2003;36:783–790.
7. Aime S, Barge A, Castelli DD, Fedeli F, Mortillaro A, Nielsen FU, Terreno E. Paramagnetic Lanthanide (III) complexes as pH-sensitive chemical exchange saturation transfer (CEST) contrast agents for MRI applications. Magn Reson Med 2002;47:639–648.
8. Keltner JR, Carlson JW, Roos MS, Wong STS, Wong TL, Budinger TF. Electromagnetic fields of surface coil in vivo NMR at high frequencies. Magn Reson Med 1991;22:467–480.
9. Slonim I, Bulai AK. Paramagnetic shift reagents in nuclear magnetic resonance. Russ Chem Rev 1973;42:904–921.
10. Parker D, Dickins RS, Puschmann H, Crossland C, Howard JAK. Being excited by lanthanide coordination complexes: aqua species, chirality, excited-state chemistry, and exchange dynamics. Chem Rev 2002;102:1977–2010.
11. Krishan K, Chang CA, Francesconi LC, Dischino DD, Malley IMF, Gougoutas JZ, Tweedle MF. Synthesis, stability, and structure of gadolinium(II1) and yttrium(II1) macrocyclic poly(amino carboxylates). Inorg Chem 1994;33:3567–3575.
12. Reilly RF. Risk for nephrogenic systemic fibrosis with gadoteridol (prohance) in patients who are on long-term hemodialysis. Clin J Am Soc Nephro 2008;3:747–751.
13. White GW, Gibby WA, Tweedle MF. Comparison of Gd(DTPA-BMA) (Omniscan) versus Gd(HP-DO3A) (ProHance) relative to gadolinium retention in human bone tissue by inductively coupled plasma mass spectroscopy. Invest Radiol 2006;41:272–278.
14. Castelli DD, Terreno E, Aime S. YbIII-HPDO3A: a dual pH- and temperature-responsive CEST agent. Angew Chem Int Ed 2011;123: 1838–1840.
15. Delli Castelli D, Caligara MC, Botta M, Terreno E, Aime S. Combined high resolution NMR and ^1H and ^{17}O relaxometric study sheds light on the solution structure and dynamics of the lanthanide(III) complexes of HPDO3A. Inorg Chem 2013;52:7130–7138.
16. Solomon I. Relaxation processes in a system of two spins. Phys Rev 1955;99:559–565.
17. Bloembergen N, Morgan LO. Proton relaxation times in paramagnetic solutions. Effects of electron spin relaxation. J Chem Phys 1960;34: 842–850.
18. Gueron M. Nuclear Relaxation in macromolecules by paramagnetic ions: a novel mechanism. J Magn Reson 1975;19:58–66.

19. Fries PH, Belorizki EJ. Quantitative interpretation of the very fast electronic relaxation of most Ln3+ ions in dissolved complexes. J Chem Phys 2012;136:074513.
20. Funk AM, Fries PH, Harvey P, Kenwright AM, Parker D. Experimental measurement and theoretical assessment of fast lanthanide electronic relaxation in solution with four series of isostructural complexes. J Phys Chem A 2013;117:905–917.
21. Ward KM, Balaban RS. Determination of pH using water protons and chemical exchange dependent saturation transfer (CEST). Magn Reson Med 2000;44:799–802.
22. Murase K, Tanki, N. Numerical solutions to the time-dependent Bloch equations revisited. Magn Reson Imag 2011;29:126–131.
23. Woessner DE, Zhang S, Merritt ME, Sherry AD. Numerical solution of the Bloch equations provides insights into the optimum design of PARACEST agents for MRI. Magn Reson Med 2005;53:790–799.

SUPPORTING INFORMATION

Additional Supporting Information may be found in the online version of this article.

SUPPORTING FIG. S1. Image of the complete pH map (a) and of the bladder ROI (b, corresponding to Figure 7); five marked pixels are located at the bladder's anatomical boundary. The apparently homogeneous pH values in the vicinity of the organ are misleading, as the voxel-by-voxel analysis (c–g) suggests. The rightmost pixel is located in the bladder (Z spectrum (c)), whereas the leftmost pixel is well outside the organ (Z spectrum (g)). The CEST signal from the pixels included in the ROI (c,d) is well quantifiable. The pixel at the boundary (e) shows CEST signal, but is filtered out with a sufficiently high quantification boundary. The Z spectra relative to the pixels furthest from the bladder (f,g) do not show any paraCEST signal.

Chapter 3

Gradient Ascent Pulse Engineering for Rapid Exchange Saturation Transfer

Journal of Magnetic Resonance 252 (2015) 1–9

Contents lists available at ScienceDirect

Journal of Magnetic Resonance

journal homepage: www.elsevier.com/locate/jmr

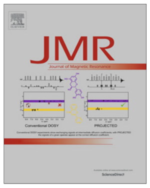

Gradient ascent pulse engineering for rapid exchange saturation transfer

G. Rancan [a,b,1], T.T. Nguyen [a], S.J. Glaser [a,*]

[a] Department of Chemistry, Technical University Munich, 4, Lichtenbergstr., Garching, Germany
[b] Klinikum rechts der Isar, Technical University Munich, 22, Ismaningerstr., München, Germany

ARTICLE INFO

Article history:
Received 11 November 2014
Revised 17 December 2014
Available online 8 January 2015

Keywords:
CEST
ParaCEST
Optimal control
GRAPE
Pulse engineering
pH
Nuclear magnetic resonance
pH mapping
Yb-HPDO3A

ABSTRACT

Efforts in the clinical translation of the paraCEST contrast agent Yb-HPDO3A have prompted an investigation into saturation pulse optimality under energy constraints. The GRAPE algorithm has been adapted and implemented for saturation pulse optimization with chemical exchange. The flexibility of the methodology, both in extracting the microscopical parameter ensemble for the algorithm as well as in determining the characteristics of this new class of rising amplitude waveforms allows rapid testing and implementation. Optimal pulses achieve higher saturation efficiencies than the continuous wave gold standard for rapid and especially for variable exchange rates, as brought about by pH-catalysis. Gains of at least 5–15% without any tradeoff have been confirmed both on a spectrometer and on a clinical imager. Pool specific solutions, with pulses optimized for a specific exchange rate value, additionally increase the flexibility of the CEST ratiometric analysis. A simple experimental approach to determine close to optimal triangular pulses is presented.

© 2015 Elsevier Inc. All rights reserved.

1. Introduction

Chemical exchange saturation transfer (CEST) MRI techniques – as first reported by Ward et al. [1,2] – generate negative contrast based on the transfer of magnetization brought about by the chemical displacement of spins. This transfer usually involves, but is not limited to [3,4], protons in aqueous media. Since its first discovery there have been efforts to extract clinically relevant physicochemical information – such as pH and temperature – through this technique. While CEST based on endogenous molecules and macromolecules is of relatively straightforward clinical application, it is necessarily limited in scope and heavily dependent on instrumental specifications. CEST from contrast media on the other hand is customizable and can be tailored to precise clinical needs, albeit being hampered by severe safety restrictions for human use. Detailed reviews on the subject are readily available in literature [5–7].

ParaCEST makes use of the paramagnetic shifting properties of selected ions to exploit rapid (10^4 Hz) exchange rates. Numerous chelates relying on the shifting properties of lanthanide nuclei benefit from the research performed on gadolinium-based relaxation agents. The well-defined molecular structures and properties of these compounds are well suited for a rational approach to CEST and the design of contrast media. The great advantage of paraCEST compounds, which can exploit high exchange rates without incurring in signal coalescence, raises some issues in the clinical setting. A rapid exchange regime means that a spin will only experience a fraction of the applied saturation RF pulse during its residence time on the chelate. Particularly continuous wave (cw) saturations are very efficient in transferring saturation, not only because of their spectral selectivity, but especially due to their high duty cycle (DC). Such RF pulses pose a problem in the clinical setting, where the RF duty cycle is restricted, and pulse trains are employed instead [8]. The second challenge when optimizing presaturation pulses on paraCEST is RF energy, related to local heating and specific absorption rate (SAR). In rapid exchanging paraCEST, the ST effect generally increases with RF amplitude, up to signal coalescence from saturation spillover at large B_1 fields. In vitro, especially at high fields, this limit does not pose an experimental problem. On the other hand, the limitations are very strict on clinical scanners [9]. The energy deposition is proportional to the square of the pulse amplitude [10] and is also field (B_0) dependent [11]. For a given external magnetic field B_0 and a maximum overall pulse energy E, the aim is to optimize the saturation transfer effect.

Among the pulse optimization procedures, the gradient ascent pulse engineering (GRAPE) [12] algorithm stands out for its simplicity and computational effectiveness. To the author's knowledge, no previous study of GRAPE on systems undergoing

---

* Corresponding author.

E-mail addresses: giaime.rancan@tum.de (G. Rancan), steffen.glaser@tum.de (S.J. Glaser).

[1] Principal corresponding author.

http://dx.doi.org/10.1016/j.jmr.2014.12.016
1090-7807/© 2015 Elsevier Inc. All rights reserved.

chemical exchange has been performed. Applying GRAPE to the Bloch equations modified for two [13] or three pool [14] chemical exchange is relatively straightforward. Optimization of the pulse under energy constraints was performed for the pH mapping para-CEST agent Yb-HPDO3A.

2. Theory

2.1. Gradient ascent pulse engineering (GRAPE)

The GRAPE algorithm [12] in its vectorial form is a conceptually simple tool for generating optimal pulses. It defines a series of rectangular RF events composing a pulse envelope and modulates their amplitude and phase in the form of u_x and u_y components of B_1. Propagating the magnetization vector means numerically solving the Bloch equations modified for chemical exchange. This can be done expeditiously by using the exponential solution for the Bloch equations in homogeneous matrix form [15], in analogy with the solution presented for the quantum mechanical formalism [16].

Let A be the homogeneous matrix (Appendix A), it is possible to define

$$U = \exp(A\tau) \tag{1}$$

as the propagator for a given time step of length τ and amplitude ω of the pulse. At cost of a higher computational load it is possible to discretize the total allotted pulse time in smaller time steps. Given the relaxation rates, RF controls and offsets, the individual propagators U_n $(1 \leqslant n \leqslant m)$ can be calculated independently. After the m-th time step, the initial magnetization M_0 will have evolved to

$$M_m = U_m \cdot \ldots \cdot U_1 \cdot M_0 \tag{2}$$

Within the simulation framework, a way of steering the pulse controls (u_x and u_y components of B_1) is needed to achieve optimality. To this end, a figure of merit to be maximized or minimized needs to be defined. A gradient is used to assess the change of the figure of merit after a small change du in controls. The changed pulse amplitude in time step n results in a modified propagator P_n, which substitutes U_n in the chain of propagation.

$${M'_m}^{\,n} = U_m \cdot \ldots P_n \cdot \ldots U_1 \cdot M_0 \tag{3}$$

The resulting vector ${M'_m}^{\,n}$ can be compared to the unmodified counterpart M_m. One figure of merit is the scalar product between the two vectors. This can be restricted to a component of the vector, for instance the longitudinal component of the water pool magnetization.

The amount by which the figure of merit Φ changes with respect to the change of the control from U_n to P_n represents the gradient. An efficient implementation of this finite difference approach is described in [17].

$$G^n = \frac{\Phi - \Phi_n}{du} \tag{4}$$

The algorithm's iterative process is provided in Appendix D. It has been implemented in Matlab, and is available as Supplementary material.

3. Methods

3.1. Modeled system

In the following, we will focus on the lanthanide-based para-CEST agent Yb-HPDO3A (Fig. 1). The compound is related to the gadolinium-based contrast agent ProHance® and consists of the same chelator, but with a high effective electronic magnetic moment (μ_{eff}) Ytterbium core. Work by the group of Aime [18–20] determined this complex apt for many innovative uses, the more interesting of which is in vivo pH and temperature mapping. Yb-HPDO3A is found in solution as a diastereomeric mixture, with conformers SAP (Square AntiPrismatic) and TSAP (Twisted Square AntiPrismatic) visible on the NMR spectrum acquired in the slow exchange regime [20]. The saturation transfer (ST) effect of the contrast agent is due to the base-catalyzed exchange of the hydroxyl proton on the complex's side chain. The vicinity of the protons to an Yb-coordinating oxygen atom produces a considerable, geometry dependent downfield shift to its Larmor frequencies. Due to the different relative geometrical positions of the exchanging proton and the Yb^{3+} core, the chemical shift from the water resonance of the two species is appreciably different: 67.37 (TSAP) and 94.26 ppm (SAP) at 310.1 K. The chemical similarity of the two species, as well as the interchange between them, allows one to regard their biodistribution as identical. This in turn opens the way to a ratiometric analysis, which makes use of both signals to circumvent the need for concentration determination of the contrast agent.

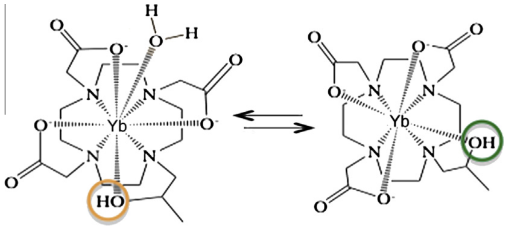

Fig. 1. Chemical formulae and representative interconversion between square antiprismatic (SAP, left) and twisted square antiprismatic (TSAP, right) Yb-HPDO3A diastereomers. The CEST effect is due to the protons on the marked hydroxyl moieties undergoing rapid exchange with water.

3.2. CEST analysis

The key goal of the ratiometric pH-CEST analysis is the possibility to obtain concentration independent information from the CEST molecule. In the seminal paper by Ward et al. [2], the ratiometric methodology was presented based on the condition:

$$M_s/M_o \approx \frac{1}{1 + C_p \cdot [CEST] \cdot \chi \cdot T_{1w}}$$

Where M_s is the indirectly saturated and M_0 the unsaturated magnetization, T_{1w} the T_1 of bulk water and C_p the exchange rate for the considered proton pool. $[CEST]$ is the agent's concentration, χ the number of exchanging sites or diastereomeric fraction, and their product is the total spin concentration of the pool. By conveniently defining the Saturation Transfer value as

$$ST := \frac{M_0 - M_s}{M_s} \tag{5}$$

it is directly proportional to the agent's concentration as well as T_1.

$$\frac{M_o - M_s}{M_s} \approx C_p \cdot [CEST] \cdot \chi \cdot T_{1w}$$

It follows that the ratio of the ST from the two pools:

$$ratio := \frac{ST^{SAP}}{ST^{TSAP}} \tag{6}$$

depends on the relative concentration of the square antiprismatic (SAP) and twisted square antiprismatic (TSAP) diastereomers (or alternatively of the exchanging sites), which are assumed constant, and the ratio of the exchange rates. It is however independent of the compound's absolute concentration as well as the T_{1w} time of the solution, provided the variation in concentration is limited.

3.3. Three pool model

The set of Bloch equations modified for three pool chemical exchange [14] was employed as a reasonable approximation to the presented chemical system. The exchange is taking place between the water pool (a) and the hydroxyl protons of the diastereomeric species b and c for TSAP (Ω_b: 67.37 ppm) and SAP (Ω_c: 94.26 ppm) respectively. No direct exchange between the two CEST pools is considered, which at low concentrations is negligible. The model also does not take into account the ring inversion interchange of the two conformers. Calculations require the input of parameters such as the frequency offsets Ω, T_1 and T_2 of the three proton pools, the exchange rates involved and the spin proportions. These parameters were obtained through fitting of experimental data to the employed model (Appendix B).

3.4. Pulse generation

The figure of merit to be maximized was defined as the saturation transfer (Eq. (5)). ST is defined based on the intensities of the water signal after saturation at the exchanging proton's frequency and without saturation. In the present setting, it corresponds to the result of on-resonance and off-resonance (symmetrical to the water resonance) irradiation. This implies running the GRAPE algorithm for the two offset frequencies and extracting the z component of the resulting water pool magnetization from each.

The guess of initial controls is a non-zero random pulse. Setting continuous wave as initial guess produced faster convergence of the algorithm. The pulse evolution over a length of 2.5 s was considered. A maximal overall value of energy (E) was kept constant ($2\pi \cdot 10^6$ rad/s for spectroscopy, $2\pi \cdot 1.157 \cdot 10^5$ rad/s for imaging):

$$E = \int (\gamma B_1)^2 dt$$

To determine pulses for the spectroscopical environment, 10 ms time steps (τ) were considered. For the clinical imaging scanner, 50 ms time steps and a 50% DC were considered. For simulations, a 50 ms time step length was used to achieve faster convergence of the algorithms, but is representative of a finer segmentation.

3.5. Experimental

Ten samples of Yb-HPDO3A 50 mM in DPBS (Dulbecco Phosphate Buffer Solution) were titrated to pH values of 5.28, 5.88, 5.92, 6.07, 6.38, 6.67, 6.81, 7.16, 7.44, 7.72, 8.03 ± 0.01 with negligible volumes of 5 M HCl and NaOH, using a calibrated S220 Sevencompact™ Mettler Toledo pH-meter. The concentration of phosphate ions is known [21] to have an effect on the rate of proton exchange. The solutions were inserted in capillaries and placed in a DMSO-d6 containing NMR tube, for field locking. For the imaging experiments, five 50 mM solutions of Yb-HPDO3A in DPBS were titrated to pH 6.0, 6.4, 6.8, 7.2, 7.6. Instrumentation and pulse sequences are described in Appendix C.

4. Results

To gain more insight into the optimization outcomes, pulses were systematically optimized in a range of key parameters (the solution's apparent T_1, exchange rates, concentration), starting from the fitting results. A common feature of the optimal pulses is a monotonically increasing amplitude as a function of time, with a maximum at the end of the saturation period. The dependence of optimal saturation pulse shapes on the apparent T_1 was investigated by varying T_{1a} (T_1 of the water pool a) in the range of 0.1–5 s (Fig. 2a and b). In general, longer relaxation times result in pulse shapes with slowly rising amplitudes. For a sufficiently long apparent T_1, the pulse shape approaches continuous wave irradiation. Using the same set of starting parameters, the exchange rates for the pool b (C_b) and pool c (C_c) were changed from 100 to 7500 Hz and 100 to 20,000 Hz respectively (Fig. 2c and d). In order to make the effect of varying exchange rates independent of changes in the apparent T_1, this value was kept constant. The minor changes in the solution's apparent T_1, stemming from variations in the exchange rates, were compensated by modulating T_{1a} responsively. For relevant concentrations above 10 mM, optimal pulses are only minimally affected by its change (data not shown).

Optimal pulse shapes for experimental tests are shown in Fig. 3. Pulse trains for imaging are composed of 50 ms block pulses on a 50% duty cycle, with a bandwidth sufficient for resolving the two highly shifted proton pools of Yb-HPDO3A.

The graphs in Fig. 4c-d show the variable amplitude same energy comparison (VASEC) plots for the two exchanging pools acquired at different pH values. The cw optimality, defined as the highest sum of ST contrast obtained in the pH range of interest (6–7.6) is 0.6 s and 1.4 s for pools c and b respectively. This finding reflects the results from the simulations in that a faster exchange benefits more from short, high amplitude pulses. At low pH values, the slower exchange regime shifts the optimal cw saturation to longer pulses. For pulse trains with constant amplitude, the VASEC plots (Fig. 5, Supplementary) show similar trends to cw. At the conditions used for imaging, the 0.4 s and 0.6 s pulse trains achieved the best overall ST for pools c and b respectively.

In the pH range of interest, the exchange rates range from 1 to 25 kHz for pool b and 6 to 80 kHz for pool c at 310 K (see Fig. 6). The fittings performed at 294 K reveal the slower rates of 0.5–2.5 kHz and 2–10 kHz for pools b and c respectively.

The optimized pulses show considerable ST gains over the cw gold standard. Fig. 7 reports the experimental gains of the optimal rising amplitude pulses over the best cw saturations, with standard deviation error bars. The gains in the imaging setting are comparable, albeit showing higher experimental errors due to the considerably lower signal-to-noise ratio.

Simulated gains (Fig. 8) show that a triangular pulse with linearly rising amplitude is a good approximation to the optimal shaped pulses in terms of saturation transfer efficiency. Both the optimal pulse and its triangular approximation are more efficient than the cw irradiation over an extended range of exchange rates. The simulated ST efficiency of the triangular approximation is above 99% of the optimal pulse, at the relevant exchange rate.

Optimized pulses can also be used to modify the pH-dependent ST response of a system. Different ST responses can be generated under the action of two distinct pulses of the same energy. This can be performed independently on both pools (Fig. 9a and b). As a result, the pH sensitivity of the method (Fig. 9c) may change considerably.

5. Discussion

The choice of the best saturation scheme is of primary importance for CEST experiments. Ideally, generating the saturation scheme should require as little experimental effort as possible. Fig. 10 summarizes the pulse determination process. VASEC plots (Fig. f10b) can be easily obtained after defining the maximum saturation energy. The proposed methodology links the pulse generation algorithm directly with the VASEC plot fitting, whithout the need for separate parameter determination. The modeling framework provided by the Bloch equations modified for chemical

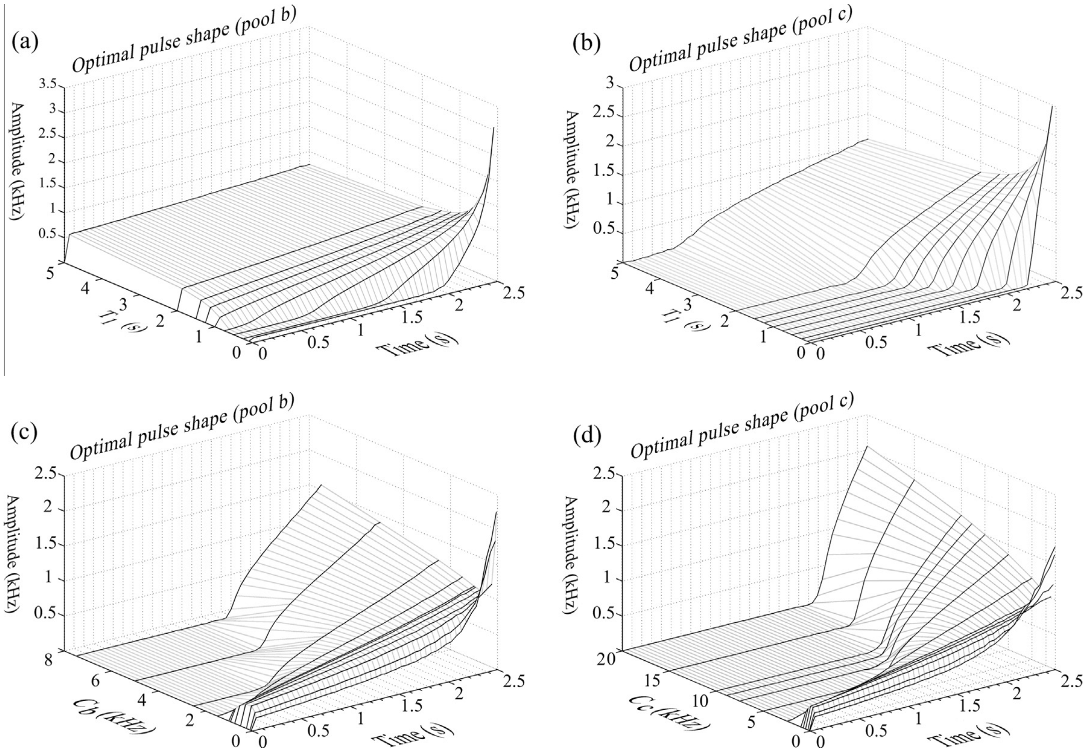

Fig. 2. Optimal pulse shapes obtained by changing a single parameter at a time. (a) In the slower exchanging pool *b* a rise in T_1 of the bulk water results in the optimal pulse approaching constant amplitude (cw irradiation). (b) Under the faster exchange conditions of pool *c* the amplitude rises rapidly at the end of the pulse evolution, even for relatively long T_1. In the range of 0.1–8 kHz (C_b) and 0.1–20 kHz (C_c), with decreasing exchange rates, the duration of non-zero irradiation increases (panels c and d). The lines connecting the pulse shapes are guides for the eye.

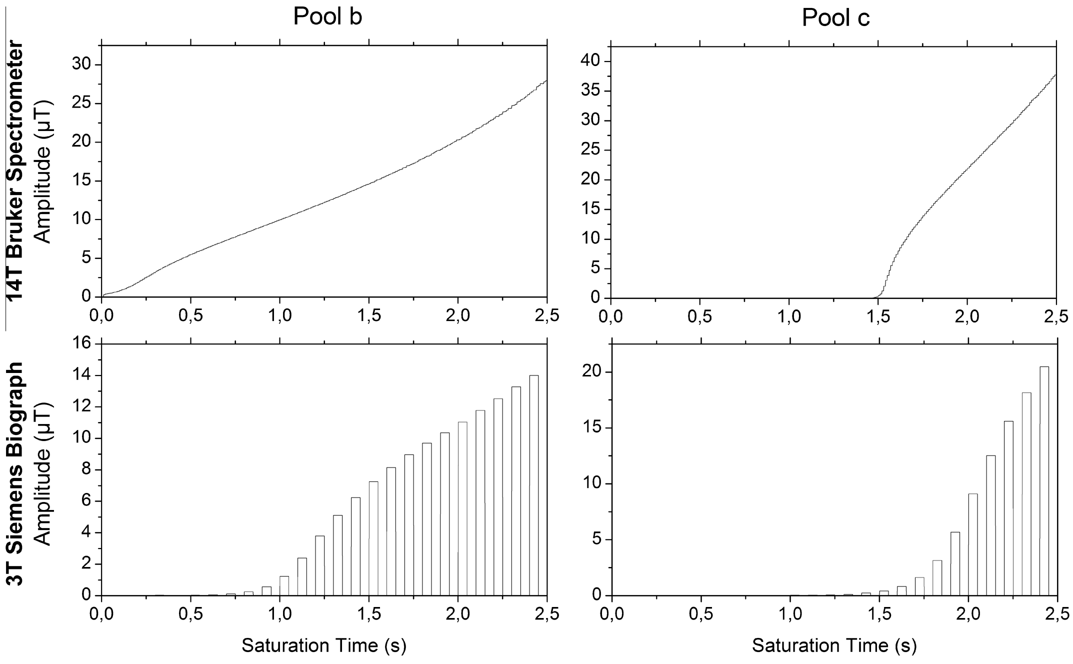

Fig. 3. Optimized continuous pulses (above) and pulse trains (below) for the two exchanging pools of the Yb-HPDO3A molecule, shifted 67.37 and 94.26 ppm from the water resonance (310.10 K). The pulses were obtained by running the optimal control algorithm on the parameters fitted from variable amplitude same energy comparison (VASEC) plots (Fig. 4), averaged in the pH range of interest (6–7.6). The saturations relative to the faster exchanging pool *c* are shorter and with a higher maximum amplitude. The pulse trains have been optimized at the SAR limit for a TR of 12 s and a patient weight of 100 kg.

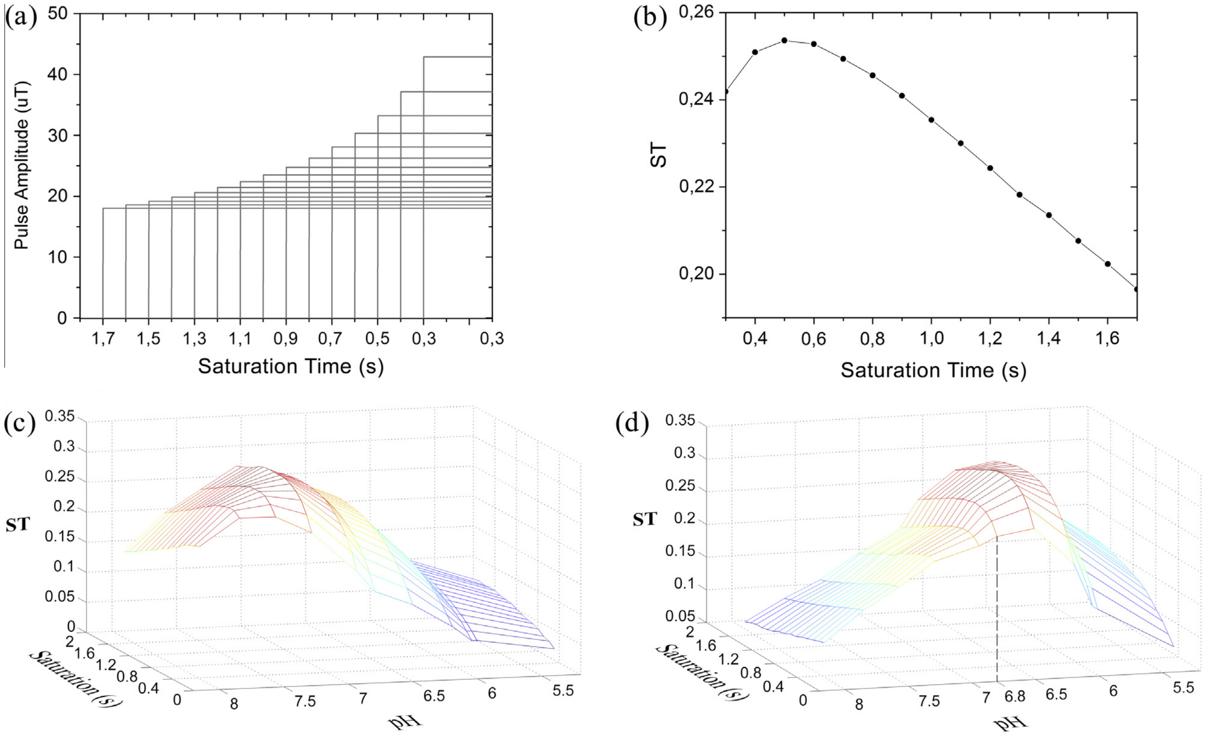

Fig. 4. Variable amplitude same energy comparison (VASEC) plots: (a) representation of the same-energy cw irradiations to be compared, (b) VASEC plot for a single pH value (6.81 for pool *c*, marked), with peak ST dependent on the choice of the irradiation, (c) VASEC plot for all pH samples for pool *b* and (d) for pool *c*. The VASEC-pH plots very clearly define the achievable ST for a given total pulse energy and are the basis of the parameter fitting for pulse optimization.

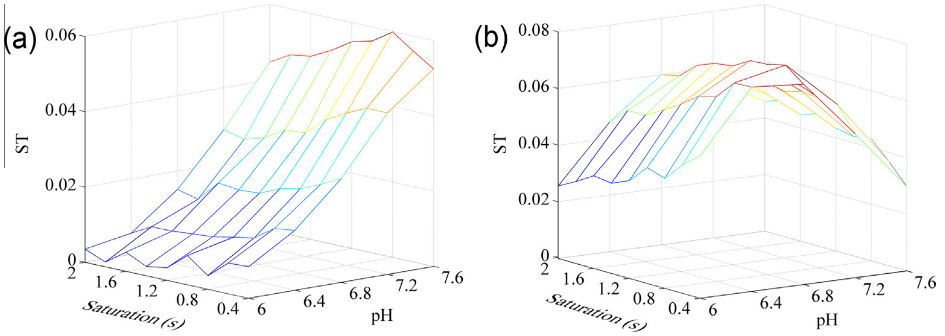

Fig. 5. VASEC plot for the saturation transfer response of pool b (left) and pool c (right), recorded at different pH values and 310.0 ± 0.5 K, on a clinical 3T Siemens Biograph. The pulse trains (50 ms BP, 50% duty cycle) have the same total energy, representing the SAR limit for the instrument (12 s TR, 100 kg patient).

exchange allows optimal control strategies to be implemented with ease. The fact that the rising amplitude optimal pulses can be approximated to triangular pulses suggests a very simple and efficient experimental approach to find close to optimal pulse shapes (Fig. 10f–h). Triangular pulses can be experimentally selected, in analogy to cw irradiations, without the need to determine microscopic system parameters and apply the GRAPE algorithm.

Rapid chemical exchange necessarily means that single spins only experience a fraction of the generated saturation pulse. Intuitively, the shorter the residence time of a spin on the CEST molecule, the larger the RF field has to be in order to generate a comparable rotation of the spins. The results from pulse optimization show the most energy-efficient solutions for saturation transfer. Rising amplitude wave outperforms continuous wave for rapidly exchanging CEST systems. In the clinical setting, where the RF duty cycle is limited, pulse trains are generated, but are conceptually equivalent to their continuous counterparts. Rapid exchanges, as typical for paraCEST agents, benefit the most from the presented treatment, because of the greater difference between cw and the resulting optimal pulse shapes. The advantages are particularly marked if the exchange rates for each pool vary greatly in the pH range of interest, as a single pulse will be employed on the different pH micromilieus in the image. Compared to cw, a single rising amplitude pulse is a better approximation to the optimal saturation for both faster or slower exchange rates.

Pulses optimized for slower or faster exchange rates will result in different pH-ST responses. This approach adds flexibility when employing a ratiometric method, and can be used to increase the pH sensitivity. The desired tradeoff between pH sensitivity and ST signal strength will depend on the instrumentation, CEST target molecules and microscopic parameters. It can be tuned by changing the pulses acting on either of the spin pools needed for the analysis.

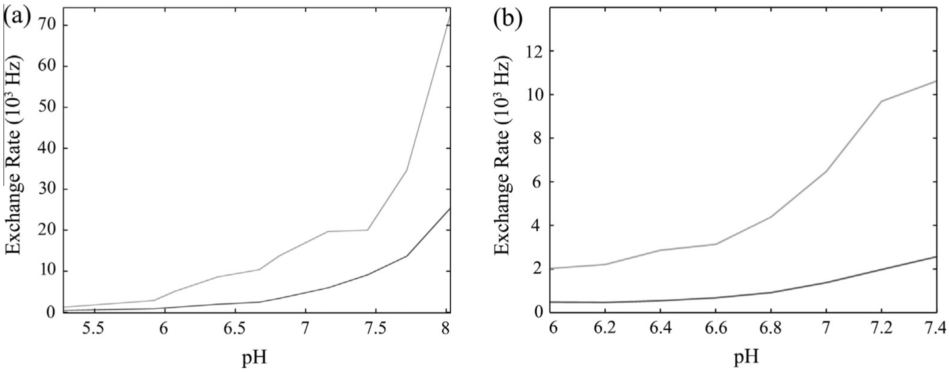

Fig. 6. Estimated exchange rates obtained from fitting of VASEC plots (Fig. 4) for (a) 310 K and (b) 294 K in DPBS. The exchange rates for pool *b* (dark gray) are considerably lower than for pool *c* (light gray). The values obtained show the strongly base-catalyzed proton exchange at different temperatures.

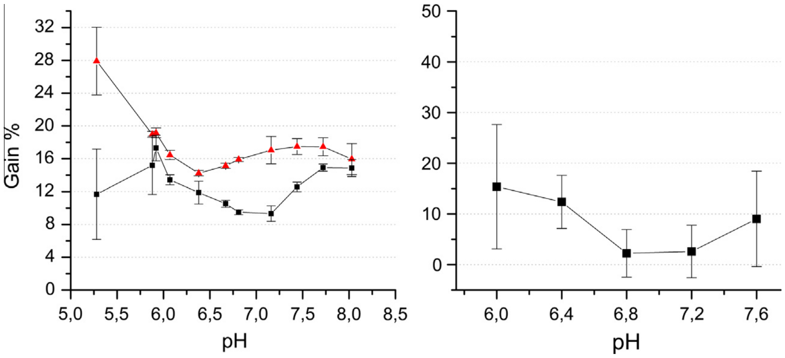

Fig. 7. Gains in ST efficiency of the optimized pulses over the best cw irradiation, defined as generating the highest total ST in the pH range from 6 to 7.6. Left, the gains obtained in spectroscopy for pool *b* (black square) and pool *c* (red triangle), with standard deviation error bars, 310.10±0.01 K, 600 MHz. Right, the gains from the proof of concept experiment on the 3T Biograph PET-MR, 310.0 K ± 0.5 K for pool *b*.

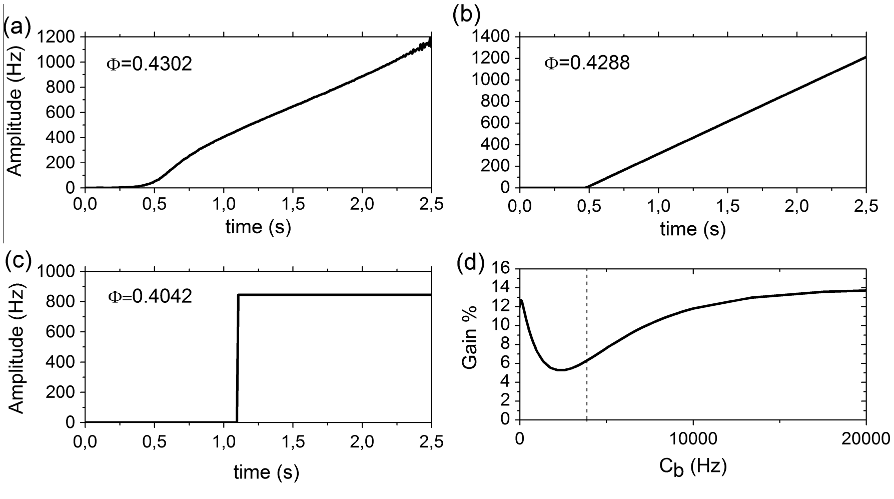

Fig. 8. (a) Optimal pulse and (c) best cw irradiation for pool *b* in the range of pH considered (6 to 7.6), as compared in the spectroscopical experiments depicted in Fig. 7. The figure of merit Φ is the simulated ST for each pulse, using the fitting parameters averaged over the pH range. The triangular pulse (b) is a good approximation to the optimal shaped pulse. (d) The simulated gains of (a) over (c) in a broader range of exchange rates of pool *b*, starting from the fitted C_b marked.

The use of multiple pulses in a ratiometric CEST experiment requires evidence that the concentration independence condition is satisfied. For long steady state inducing pulses, this approximation holds true for a large variation in concentration. Simulations confirm the expected concentration independence with the pulses presented. A deviation of the ratiometric value below 1% is found numerically at the extremes of a ±5 mM concentration range. The inaccuracy increases considerably for broader concentration ranges.

Deviation from steady state conditions requires additional validation of the employed data analysis, especially in vivo. The translation of the presented technique to diaCEST systems would need

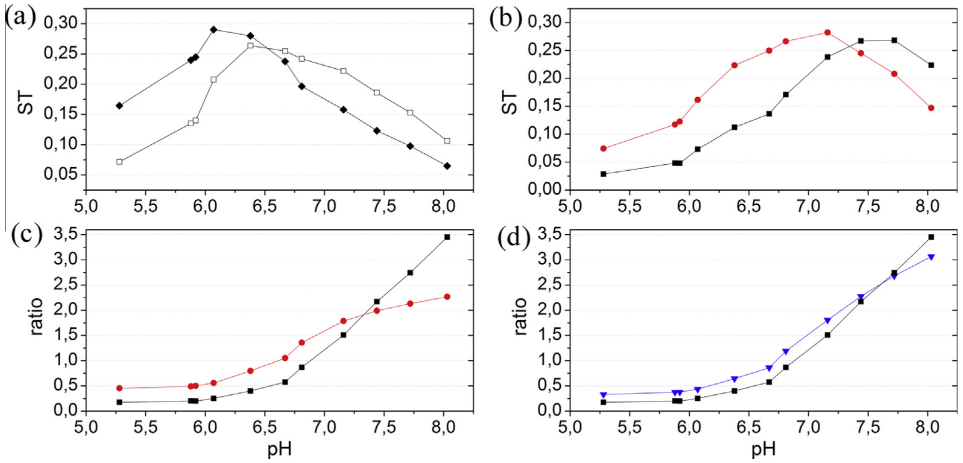

Fig. 9. Different ST responses for (a) pool *c* and (b) pool *b* obtained by using two different cw irradiations with the same energy. By modifying the pH response of the pools involved in the ratiometric analysis, the pH sensitivity changes. (c) The ratiometric plot using two sets of pulses (where the black line ST response in (a) was used with the ST responses from (b)) underlines the possible differences in pH sensitivity as well as the range of pH where it is optimal. Although a tradeoff is necessary between pH sensitivity and overall ST signal strength, optimality is always to be achieved with the class of shaped pulses presented. (d) A pH sensitivity similar to the black line in (c), obtained with optimal pulses (blue triangles) is accompanied by a 10.4% and 41.2% overall signal increase for pools *c* and *b* respectively. (For interpretation of the references to color in this figure legend, the reader is referred to the web version of this article.)

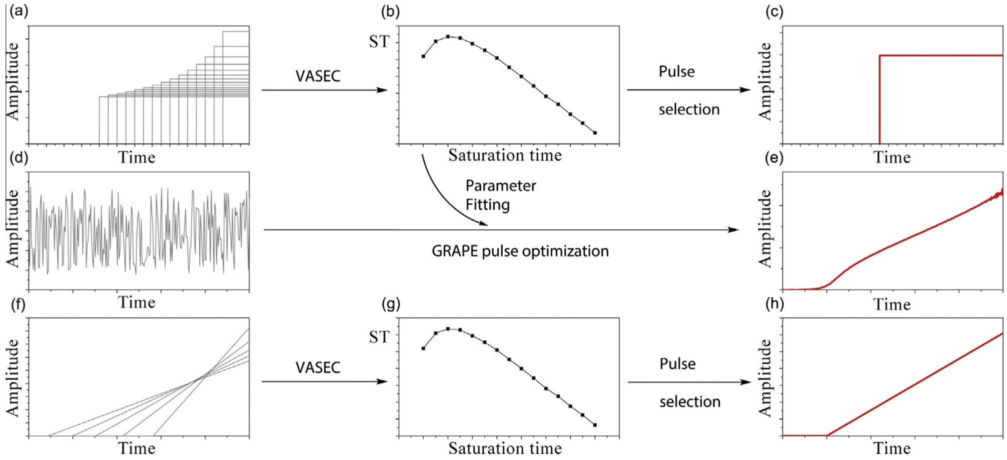

Fig. 10. Pulse selection process. (a) Same energy rectangular pulses are compared in (b) VASEC plots and (c) the most efficient (in a desired pH range) is selected. GRAPE pulse optimization starts from a (d) random pulse, or an educated guess, and employs the VASEC data for parameter determination to obtain (e) the numerical optimized pulse. (h) Triangular approximations to the resulting pulse shapes can be experimentally determined through VASEC plots in analogy to (a–c) the rectangular pulses.

$$\begin{bmatrix} 0 & 0 & 0 & 0 & 0 & 0 & 0 & 0 & 0 & 0 \\ 0 & -(R_{2a}+C_a) & -\Omega_a & 0 & C_b & 0 & 0 & C_c & 0 & 0 \\ 0 & \Omega_a & -(R_{2a}+C_a) & -\omega_1(m) & 0 & C_b & 0 & 0 & C_c & 0 \\ M_a^0 \cdot R_{1a} & 0 & \omega_1(m) & -(R_{1a}+C_a) & 0 & 0 & C_b & 0 & 0 & C_c \\ 0 & C_{ab} & 0 & 0 & -(R_{2b}+C_b) & -\Omega_b & 0 & 0 & 0 & 0 \\ 0 & 0 & C_{ab} & 0 & \Omega_b & -(R_{2b}+C_b) & -\omega_1(m) & 0 & 0 & 0 \\ M_b^0 \cdot R_{1b} & 0 & 0 & C_{ab} & 0 & \omega_1(m) & -(R_{1b}+C_b) & 0 & 0 & 0 \\ 0 & C_{ac} & 0 & 0 & 0 & 0 & 0 & -(R_{2c}+C_c) & -\Omega_c & 0 \\ 0 & 0 & C_{ac} & 0 & 0 & 0 & 0 & \Omega_c & -(R_{2c}+C_c) & -\omega_1(m) \\ M_c^0 \cdot R_{1c} & 0 & 0 & C_{ac} & 0 & 0 & 0 & 0 & \omega_1(m) & -(R_{1c}+C_c) \end{bmatrix}$$

Fig. 11. Homogeneous matrix *A*. Ω_a, Ω_b, Ω_c are the offsets (rad/s) for the three exchanging pools *a*, *b* and *c* respectively. $\omega_1(m)$ is the pulse amplitude at time step m, R_{1n} and R_{2n} the relaxation rates of the respective pools, M_n^0 their thermal equilibrium magnetization. C_n are the rates of spin exchange leaving pool *n*, with $C_a = (C_{ab} + C_{ac})$.

to address competing saturation spillover and magnetization transfer (MT) effects. These would also need to be addressed in low-field and high-power paraCEST studies. For direct saturation, particular care should be put in the optimization of phase modulated pulses (Appendix E). Ultimately, the minor competing effects in the paraCEST environment make pH mapping particularly appealing, mainly due to error propagation during the ratiometric analysis.

6. Conclusion

The quantification of an important physiological parameter such as pH is performed elegantly by ratiometric CEST techniques. Rapid exchanging paraCEST agents are prominent in this field because of the well-defined molar proportions and customizability of the desired properties they present.

Knowing the microscopic parameters of a system in a given physico-chemical condition is necessary for numerical pulse optimization. This can be achieved with ease through the presented VASEC plot fitting. The generated pulses are defined by rising amplitude profiles, mainly dependent on the exchange rate and T_1 of the bulk water. Alternatively, optimization can be performed experimentally with different triangular pulses (Fig. 10f), without the need to apply the GRAPE algorithm.

The application of optimal control theory to this class of contrast agents underlines the possibility of exploiting significant changes in exchange rates to improve sensitivity to pH. For rapidly exchanging systems, the presented class of shaped saturation pulses offers considerable gains in signal strength over conventional cw irradiation. It also opens the door to vast experiment customization possibilities, and will aid the rational design of new paraCEST agents.

Despite cw saturation not being the most energy efficient solution, a high duty cycle is however always advantageous for rapid chemical exchange. In the clinical setting, conceptually equivalent rising amplitude pulse trains can be used instead.

Acknowledgements

The project has been carried out with the support of the Technische Universität München – Institute for Advanced Study, funded by the German Excellence Initiative. The authors also acknowledge BRACCO Imaging S.p.A for providing the HPDO3A ligand and the group of Prof. Silvio Aime for scientific exchange.

Appendix A. Homogeneous matrix A

See Fig. 11

Appendix B. Fitting and parameter determination

Parameter determination was performed by fitting experimental VASEC plots (Fig. 4b). These are the plots of peak ST values obtained with different cw saturations, having varying amplitude and length, but same total energy (Fig. 4a). The VASEC plot guarantees the extraction of the most important information for pulse optimization purposes. Fittings were performed using Matlab's lsqcurvefit function and achieved high fidelity. The boundary conditions for the fit were narrowed according to available literature and experimental data [19]. The T_1 and T_2 of the water pool were measured in a slow exchange regime at pH 4, 310 K, 600 MHz through common IR (Inversion Recovery) and CPMG (Carr Purcell Meiboom Gill) sequences. The results, T_1: 0.954 ± 0.027 s and T_2: 0.342 ± 0.002 s were set as starting conditions to the fitting algorithm. The fittings were performed over the entire pH range. An average of the obtained fitting parameters over pH 6–7.6 was used for pulse generation and can be found in the released matlab script.

Appendix C. Instruments, pulse sequence

The employed spectrometer is a Bruker 600 MHz running Topspin 3.2. The temperature was kept at a stable 310.10 ± 0.01 K. The acquisition sequence involved the presaturation pulse, followed by a spoiler gradient, and a small flip angle excitation at the water frequency. A delay time of 7 s was sufficient for relaxation. For VASEC plots, three separate and alternate irradiations were performed on- and off-resonance, under the action of a set of 15 different continuous wave irradiations. The total energy was kept constant for all irradiations involved, the length of the pulses was changed from 0.3 to 1.7 s through 0.1 s increments (Fig. 4a). Conversion of pulse amplitudes into dB was performed using standard protocol, with input values as follows: 61.3 W amplifier power, instrumental 90 calibration at 7.9 us/−8 dB, under the assumption of amplifier linearity. Data analysis, fitting and the GRAPE algorithm were performed on Matlab R2012a. To avoid radiation damping effects [23], in addition to a small filling factor, a very small excitation flip angle was chosen. Additionally, the first point of the FID was used as a measure of signal intensity, avoiding the need for a readout gradient. The imaging experiments were performed on Siemens Biograph 3T (123.19 MHz) PET/MR scanner running VB18P using the mMR Head/Neck coil. A TSE sequence modified with a custom CEST SBB was used. A constant amplitude or rising amplitude pulse train of 50 ms block pulses with a 50% duty cycle and spoiler gradients during mixing time was played out before acquisition. The length of the pulse trains was varied from 0.4 to 2.0 s though 0.2 s increments.

Imaging acquisition parameters were: 64 turbo factor with a 64x64 matrix covering 150 mm isoFOV and 2 mm slice thickness. TR 12 s, TE 13 ms, 1 average. Frequencies were sampled by 101 scans, evenly spaced in the 7000–14,000 Hz offset range on either side of the water resonance. B_0 correction was performed after a WASSR acquisition of 21 frequencies in the range of ±700 Hz from water. Temperature control was obtained by circulating heated water around the samples, and kept at 310.0 ± 0.5 K.

Appendix D. GRAPE iterative process

1. Guess the initial controls ω_n.
2. Calculate the Propagators U_n through Eq. (1) and, by applying a change in control du, P_n.
3. Calculate the magnetization M_m as in Eq. (2)
4. Calculate the final magnetizations for all timesteps M_m^m, Eq. (3).
5. Evaluate the gradient with Eq. (4) for each τ and update the control amplitudes.
6. Go to (2).
7. Stop when the total gain in the figure of merit is below a desired threshold value.

Appendix E. Phase-modulated CEST pulse optimization

In the figure of merit (Eq. (5)) used for the optimizations, the difference of the water z magnetization for on- and off-resonance irradiation is considered in order to avoid a direct excitation of the water signal (spillover effect). Relative to the water resonance, the on- and off-resonance irradiation frequencies are Ω and $-\Omega$, respectively. For the case of pulses with only a single RF component (e.g. pulses with $u_y = 0$), the resulting water z magnetization is identical for Ω and $-\Omega$ if the pulse is applied to thermal equilibrium magnetization. Note that in general this is not the case for phase-modulated pulses, where both $u_x \neq 0$ and $u_y \neq 0$. However, if the pulse sequence irradiated at $-\Omega$ is derived from the original pulse by reversing the signs of all pulse phases, it is guaranteed that both pulses create the same z component of the water signal. This is a direct consequence of the fact that the overall propagator of a phase-inverted pulse is identical to the propagator of the same pulse at the negative offset plus a preceeding and following 180°_x rotation [23]. Hence, in optimizations of phase-modulated pulses, the sign of all pulse phases were inverted for the off-resonance sequence irradiated at offset $-\Omega$ relative to the water signal. As phase-modulated pulses did not lead to increased CEST performance for the spin system parameters considered here for the case of paraCEST, the presented results were all based on the optimization of a single RF component.

Appendix F. Supplementary material

Supplementary data associated with this article can be found, in the online version, at http://dx.doi.org/10.1016/j.jmr.2014.12.016.

References

[1] K.M. Ward, A.H. Aletras, R.S. Balaban, A new class of contrast agents for MRI based on proton chemical exchange dependent saturation transfer (CEST), J. Magn. Reson. 143 (2000) 79–87, http://dx.doi.org/10.1006/jmre.1999.1956.

[2] K.M. Ward, R.S. Balaban, Determination of pH using water protons and chemical exchange dependent saturation transfer (CEST), Magn. Reson. Med. 44 (5) (2000) 799–802. http://onlinelibrary.wiley.com/doi/10.1002/1522-2594%28200011%2944:5%3C799::AID-MRM18%3E3.0.CO;2-S/abstract.

[3] A. Bar-Shir, A.A. Gilad, K.W.Y. Chan, G. Liu, P.C.M. van Zijl, J.W.M. Bulte, M.T. McMahon, Metal ion sensing using ion chemical exchange saturation transfer 19F magnetic resonance imaging, J. Am. Chem. Soc. 135 (33) (2013) 12164–12167, http://dx.doi.org/10.1021/ja403542g.

[4] L. Schröder, T.J. Jowery, C. Hilty, D.E. Wemmer, A. Pines, Molecular imaging using a targeted magnetic resonance hyperpolarized biosensor, Science 314 (5798) (2006) 446–449, http://dx.doi.org/10.1126/science.1131847.

[5] M. Zaiss, P. Bachert, Chemical exchange saturation transfer (CEST) an MR *z*-spectroscopy in vivo: a review of theoretical approaches and methods, Phys. Med. Biol. 58 (2008) 221–269, http://dx.doi.org/10.1088/0031-9155/58/22/R221.

[6] E. Terreno, D. Delli Castelli, S. Aime, Encoding the frequency dependence in MRI contrast media: the emerging class of CEST agents, Contrast Media Mol. I. 5 (2010) 78–98, http://dx.doi.org/10.1002/cmmi.369.

[7] P.C.M. van Zijl, N.N. Yadav, Chemical exchange saturation transfer (CEST): what is in a name and what is not?, Magn Reson. Med. 65 (4) (2011) 927–948, http://dx.doi.org/10.1002/mrm.22761.

[8] P.Z. Sun, T. Benner, A. Kumar, A.G. Sorensen, Investigation of optimizing and translating pH-sensitive pulsed-chemical exchange saturation transfer (CEST) imaging to a 3T clinical scanner, Magn. Reson. Med. 60 (4) (2008) 834–841, http://dx.doi.org/10.1002/mrm.21714.

[9] Y. Takayama, T. Yoshiura, A. Nishie, T. Nakayama, M. Hatakenaka, N. Kato, S. Yoshise, J. Keupp, D. Burdinski, H. Honda, Ytterbium-based PARACEST agent: feasibility of CEST imaging on a clinical MR scanner, Magn. Reson. Med. Sci. 11 (1) (2012) 35–41, http://dx.doi.org/10.2463/mrms.11.35.

[10] International Commission on Non-Ionizing Radiation Protection (ICNIRP), Guidelines for limiting exposure to time-varying electric, magnetic and electromagnetic fields (up to 300 GHz), Health Phys. 74 (4) (1998) 494–522.

[11] J.R. Keltner, J.W. Carlson, M.S. Roos, S.T.S. Wong, T.L. Wong, T.F. Budinger, Electromagnetic fields of surface coil in vivo NMR at high frequencies, Magn. Reson. Med. 22 (1991) 467–480.

[12] N. Khaneja, T. Reiss, C. Kehlet, T. Schulte-Herbrüggen, S.J. Glaser, Optimal control of coupled spin dynamics: design of NMR pulse sequences by gradient ascent algorithms, J. Magn. Reson. 172 (2005) 296–305, http://dx.doi.org/10.1016/j.jmr.2004.11.004.

[13] H.M. McConnell, Reaction rates by nuclear magnetic resonance, J. Chem. Phys. 28 (3) (1958) 430–431, http://dx.doi.org/10.1063/1.1744152.

[14] D.E. Woessner, S. Zhang, M.E. Merritt, A.D. Sherry, Numerical solution of the Bloch equations provides insights into the optimum design of PARACEST agents for MRI, Magn. Reson. Med. 53 (4) (2005) 790–799, http://dx.doi.org/10.1002/mrm.20408.

[15] K. Murase, N. Tanki, Numerical solutions to the time-dependent Bloch equations revisited, Magn. Reson. Imag. 29 (1) (2011) 126–131, http://dx.doi.org/10.1016/j.mri.2010.07.003.

[16] M.H. Levitt, L. Di Bari, The homogeneous master equation and the manipulation of relaxation networks, Bull. Magn. Reson. 16 (92) (1994) 94–114.

[17] P. de Fouquieres, S.G. Schirmer, S.J. Glaser, I. Kuprov, Second order gradient ascent pulse engineering, J. Magn. Reson. 212 (2011) 412–417, http://dx.doi.org/10.1016/j.jmr.2011.07.023.

[18] D. Delli Castelli, E. Terreno, S. Aime, YbIII-HPDO3A: a dual pH and temperature responsive CEST agent, Angew. Chem. Int. Ed. 50 (8) (2011) 1798–1800, http://dx.doi.org/10.1002/anie.201007105.

[19] D. Delli Castelli, G. Ferrauto, J.C. Cutrin, E. Terreno, S. Aime, In vivo maps of extracellular pH in murine melanoma by CEST-MRI, Magn. Reson. Med. 71 (1) (2014) 326–332, http://dx.doi.org/10.1002/mrm.24664.

[20] D. Delli Castelli, M.C. Caligara, M. Botta, E. Terreno, S. Aime, Combined high resolution NMR and 1H and 17O relaxometric study sheds light on the solution structure and dynamics of the lanthanide(III) complexes of HPDO3A, Inorg. Chem. 52 (12) (2013) 7130–7138, http://dx.doi.org/10.1021/ic400716c.

[21] E. Liepinsh, G. Otting, Proton exchange rates from amino acid side chains – implications for image contrast, Magn. Reson. Med. 35 (1) (1996) 30–42, http://dx.doi.org/10.1002/mrm.1910350106.

[23] V.V. Krishnan, N. Murali, Radiation damping in modern NMR experiments: progress and challenges, Prog. Nucl. Mag. Res. Sp. 68 (2013) 4157, http://dx.doi.org/10.1016/j.pnmrs.2012.06.001.

[23] M.H. Levitt, Composite pulses, Prog. Nucl. Mag. Res. Sp. 18 (1986) 61–122, http://dx.doi.org/10.1002/9780470034590.emrstm0086.

Chapter 4

Liposomial drug delivery system: characterization of encapsulated Yb-HPDO3A

4.1 Introduction

The chemical exchange saturation transfer (CEST) effect relies on saturation being transferred from chemically shifted protons to the water via spin exchange. The negative contrast generated upon acquisition of a spin density image is usually limited, and sensitivity is a major concern for this methodology.

Contrast agent mediated CEST effects rely on a sufficient concentration of the chemically shifted spins reaching the anatomical target. Low concentrations can be compensated by faster proton exchange rates. However, this is only true when the chemical shift and the applied irradiation amplitude are sufficiently high. In practice, the conditions are fulfilled for paraCEST agents on preclinical instruments. In the clinical setting, some paraCEST compounds may also find use at low (<1.5T) field, where SAR constraints are less limitating.

Yb-HPDO3A is a paraCEST agent that showed some promise for pH mapping on high field preclinical imagers (57). Pulse optimization showed CEST contrast gains being achievable by the use of rising amplitude continuous saturation, at the cost of not reaching a steady-state (Chapter 3).

A further strategy that might be pursued is that of drug delivery systems. Liposomes are especially interesting for CEST (22), yet add complexity to the paraCEST analysis. As reported by Delli Castelli et al. (81), an inhomogenoeus distribution of paramagnetic ions, such as those incapsulated in high concentration by liposomes, leads to a shortening of the T_2 time of the solution. A short T_2 time increases unwanted saturation spillover and decreases the CEST labeling efficiency, the effects being strongly related to the B_0 field strength (Section 1.8).

4.2 Methods

The liposomes were prepared from a chloroform solution containing POPC ($\chi = 0.80$), DSPE-mPEG2000 ($\chi = 0.05$) and Cholesterol ($\chi = 0.15$), then extruded (4-pass 400/200/100 nm membranes at 37°C) to SUVs of 120 nm mean diameter (PDI<0.05). The liposomial film was hydrated with solutions containing increasing concentrations of Yb-HPDO3A (50, 100, 150, 200, and 300 mM) taken to 300 mOsm with NaCl. Dialysis was performed with an iso-osmolar HEPES buffer at pH 7.3 in two steps (4 hrs, overnight).

Liposomial characterization was performed through the following: Evans method (at 290.0 K), Z spectra at single or variable pH (at 310.1 K), T_2 measurement (CPMG sequence, at 290.0 K) and variable amplitude single-resonance CEST experiments. All NMR measurements were performed on a Bruker 600 MHz spectrometer at 310.1 K. CEST presaturation consists of CW irradiation at 24 μT (90°: 7.4 us/-3 dB, Amplifier Power: 50 W) for 3 s, with the exception of the variable amplitude experiment.

The release of the paraCEST agent from the liposomes was induced by sonication (20 kHz, 49 W, 5 min) for direct Z spectra comparison. Liposomial stability was assessed by repeating T_2 measurements on a daily or weekly basis. The liposomes have proven stable for at least 6 days at 37°C and 90 days at 4°C.

4.3 Results

The T_2 effect of the analysed solutions is a function of both the overall concentration of the paramagnetic compound and how homogeneously it is distributed in the sample. The difference between the liposomial and free (after sonication) T_2 contributions is considerable ($T_2^{free}/T_2^{Lipo} = 35$ for the 200 mM loading), and it can be used as a marker to assess the stability of the nanoparticle. However, the loading-dependent T_2 shortening (and the less dramatic T_1 shortening) can result in a CEST signal quench. As shown in figure 4.1, the liposome with a 300 mM Yb-HPDO3A loading produces a much lower ST signal than its free counterpart. What can also be noticed from the Z spectrum is the difference of the TSAP signal's chemical shift between the liposomial and free forms. The shift is concentration-dependent and was confirmed in 1D proton spectra. It is likely due to conformational changes brought about by variations in the intermolecular bonding.

For the irradiation conditions stated before, up to 200 mM, the faster exchanging SAP pool (shifted ca. 94 ppm from water) displays only a small signal reduction. The results are summarized in Table 4.1.

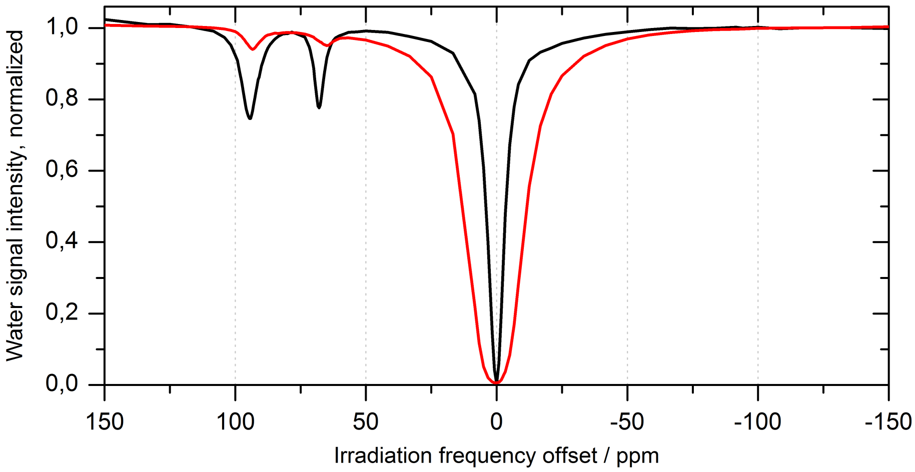

Figure 4.1: Z spectra obtained from the 300 mM Yb-HPDO3A loaded liposome (red), showing a marked reduction of the ST effect to the free solution of Yb-HPDO3A (black) due to increased relaxation rates. The free solution was obtained by sonicating the liposomes, thereby maintaining the total concentration and pH constant. The acquisition was performed at 310.1 K, with *cw*-presaturation of 3 s and 24 μT amplitude. The difference in the direct saturation of water is also attributable to the increased relaxation rates, especially T_2. The additional paramagnetic contributions result from an inhomogenoeus distribution of the Yb^{3+} ions in the sample.

The Evans shift method uses the paramagnetic-induced shift δ_j^{bulk} affecting the tBuOH - relative to a reference - to determine the concentration of the paramagnetic species.

$$\delta_j^{bulk} = (\frac{\mu_{eff}}{2.828})^2 \cdot \frac{s_f \cdot c}{T} \cdot 10^3$$

where μ_{eff} is the effective electronic magnetic moment (Yb = 4.3), the constant $2.828 = \sqrt{(\frac{3k_B}{N_A\mu_B^2})}$, s_f is the shape factor of the magnet ($4\pi/3$ for a cylindrical sample), c is the molarity of the paramagnetic compound and T the absolute temperature (290.0 K).

The highest liposome loading concentration for which no dramatic relaxation quench was witnessed at 24 μT is 200 mM. The ST signal is greatly dependent on the irradiation amplitude, and the signal intensity of the faster exchanging SAP isomer was tested experimentally with different saturation amplitudes. Figure

Loading (mM)	tBuOH shift (ppm)	ST_{lipo}^{SAP}	ST_{free}^{SAP}	TSAP shift (ppm)
50	0.096	0.085	0.095	0.83
100	0.167	0.145	0.130	1.25
150	0.133	0.108	0.143	1.67
200	0.214	0.194	0.211	2.08
300	0.319	0.060	0.253	2.92

Table 4.1: Collected experimental data for the paraCEST liposomes at different loading concentrations. The Evans method is based on the tBuOH shift in the solution and is used to calculate the effective paramagnetic concentration, therefore reporting on the liposomial concentration. The Saturation Transfer effect of the faster exchanging SAP isomer is similar, within experimental error, in the free and liposomial forms up to 200 mM loading, under the described experimental conditions. The concentration dependent shift of the TSAP peak is most likely due to conformational changes.

4.2 presents a plot of the ST^{SAP} as a function of the irradiation amplitude for the liposomial and free solutions. Up to 12 μT, the magnitude of the saturation transfer signal is the same. At higher irradiation frequencies, the liposomial CEST signal is considerably lower than the solution of free Yb-HPDO3A. The effect can be ascribed to the shortening of the T_1 and T_2 times for the proton pools involved in the chemical exchange, which can be easily simulated with the Bloch-McConnell equations.

While limited water exchange across the membrane may also quench the CEST signal, there is no simple way to discriminate the effect from relaxation-based quenching. A different, non-paramagnetic system with fast exchanging protons would be required for that purpose.

With a viable system (200 mM loaded liposome) and experimental conditions (12 μT, 310.1 K) established, an additional step to prove the viability of a Yb-HPDO3A liposomial drug delivery system is its pH response. The flow of water molecules across the very fluid POPC-rich membrane does not need additional proof, and the exchange of hydronium and hydroxide ions is given by to the Grotthuss mechanism. On the other hand, the passage of the counterions and pH equilibration needs to be proven, as the pH sensitivity of the system would be affected.

Figure 4.3 reports the pH sensitivity for three different irradiation amplitudes. For 12 μT, the pH sensitivity is optimal between 6.6-7.8. At higher saturation amplitudes it is shifted towards higher pH values. There is no reason to believe that the pH does not equilibrate across the membrane. It appears to be that the pH range to which

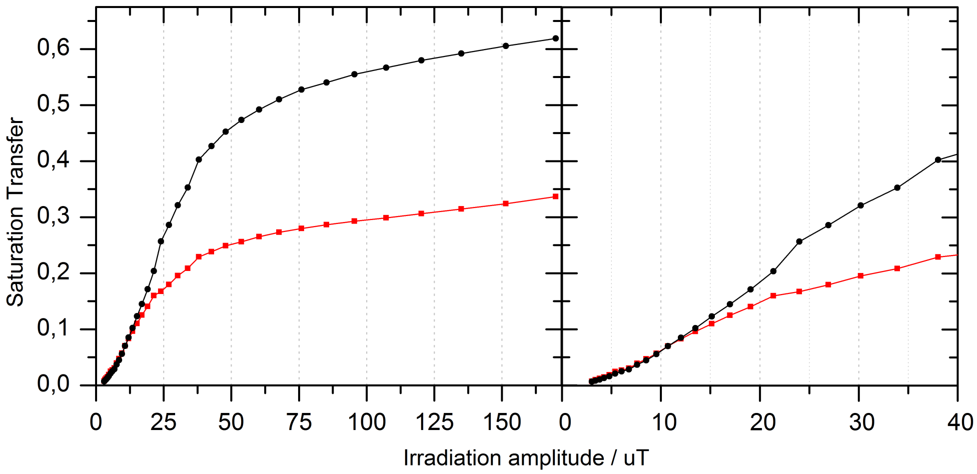

Figure 4.2: Plot of the ST signal for the faster exchanging SAP diastereomer with variable irradiation power. The saturation was performed with a *cw*-irradiation at variable amplitude for 3 s. The plot on the right hand side highlights a smaller, experimentally more relevant, interval of amplitudes. The ST effect achieved by the liposomial formulation (red) of 200 mM loading is lower than for the free Yb-HPDO3A (black) at amplitudes higher than approximately 12 μT.

the system offers optimal sensitivity is affected by the relaxation quench in addition to the saturation amplitude used, albeit not dramatically (data on the sonicated samples is not shown). On the contrary, the magnitude of the pH sensitivity is reduced by relaxation quenching at higher saturation amplitudes.

4.4 Discussion and conclusions

The CEST effect relies on intermolecular proton movement. As such, there are conditions where a limited diffusivity of the main saturation carrier (the water) results in a reduced labeling efficiency. For lipoCEST systems, where a separate proton pool is a desired outcome, a rate-limiting lipid bilayer membrane is required. For drug delivery of CEST agents, especially those with fast exchange rates such as Yb-HPDO3A, a rate-limiting membrane is unwanted. Liposomial relaxation agents based on paramagnetic loading might also benefit from more permeable membranes. The liposomial composition used in this work allows free spin exchange in the presented experimental conditions. The sensitivity to pH was largely unaffected

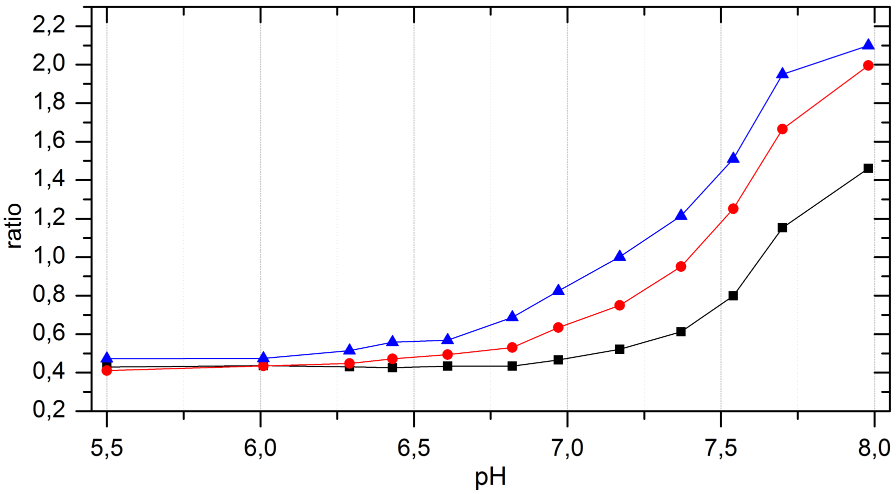

Figure 4.3: Ratiometric curves displaying the pH sensitivity of the 200 mM Yb-HPDO3A loaded liposomes after a 3 s *cw*-irradiation at 11.9 (blue), 23.7 (red) and 53.1 (black) μT, 310.1 K. The optimal pH sensitivity at higher saturation amplitudes is shifted towards the faster exchange rates at higher pH.

by the presence of the bilayer membrane. It changed, naturally, with the applied irradiation amplitude - as discussed in chapter 3.

The major drawback to Yb-based paraCEST drug delivery systems appears to be T_2 quenching. The effect is more dramatic at the high field the present study was conducted. At 600 MHz, the liposome loaded with 200 mM Yb-HPDO3A showed no signal quenching up to 12 μT irradiation amplitude. The result is encouraging, as SAR constraints for clinical use are more restrictive.

At the lower fields where paraCEST may prove clinically relevant, it is safe to assume that a higher loading can be achieved, and higher irradiation amplitudes employed without signal loss. Care should be placed in the spillover correction, as a result of T_2 broadening of the baseline. For Yb-HPDO3A, a ratiometric method between its T_2 effect and ST can be envisioned. Other paramagnetic ions with a more pronounced relaxation enhancement should only be tested at low field.

Appendix A

On the Bloch equation

See "Magnetic Resonance Imaging: Physical Principles and Sequence Design." (82)

For uncoupled spin 1/2 systems, a magnetization vector representation is sufficiently accurate. By defining the magnetization vector as $\boldsymbol{M} = (M_x, M_y, M_z)$, in a static magnetic field $\boldsymbol{B} = (0, 0, B_0)$, $\boldsymbol{M}$ will align with $\boldsymbol{B}$ in order to minimize its potential energy $U = -\boldsymbol{M} \cdot \boldsymbol{B}$. This process happens by energy transfer to the lattice in form of thermal motion. The normalized equilibrium value is $\boldsymbol{M} = (0, 0, 1)$. The rate of change of the longitudinal magnetization can be described as:

$$\frac{dM_z(t)}{dt} = (M_0 - M_z)/T_1$$

where T_1 is the experimentally derived longitudinal relaxation time. After solving the differential equation, the exponential character of the regrowth is clear.

$$M_z(t) = M_z(0)e^{-t/T_1} + M_0(1 - e^{-t/T_1})$$

The relaxation of the transverse magnetization to its equilibrium value is described by

$$\frac{d\boldsymbol{M}_\perp}{dt} = \gamma \boldsymbol{M}_\perp \times \boldsymbol{B} - \boldsymbol{M}_\perp/T_2$$

with $\boldsymbol{M}_\perp = M_x\hat{x} + M_y\hat{y}$.

In the rotating frame, the effective field condition applies:

$$\boldsymbol{B_{eff}} = (B_0 - \frac{\omega_0}{\gamma}\hat{z})$$

with $\omega_0 = \gamma B_0$. Thus,

$$\frac{d\boldsymbol{M}_\perp}{dt} = -\boldsymbol{M}_\perp/T_2$$

The solution is also an exponential regrowth.

$$\boldsymbol{M}_\perp(t) = \boldsymbol{M}_\perp(0)e^{-t/T_2}$$

In the presence of an additional B_1 field, as generated by an RF pulse, the effective field in the rotating frame is:

$$\boldsymbol{B_{eff}} = (B_0 - \frac{\omega_0 - \Delta\omega}{\gamma})\hat{z} + \frac{\omega_1}{\gamma}\hat{x}$$

or

$$\boldsymbol{B_{eff}} = (\boldsymbol{\frac{\omega_1}{\gamma}, 0, \frac{\Delta\omega}{\gamma}})$$

with $\Delta\omega = \omega_0 - \omega$.

Considering the composition of the previously defined differential equations:

$$\frac{d\boldsymbol{M}}{dt} = \gamma \boldsymbol{M} \times \boldsymbol{B_{eff}} + \frac{(M_0 - M_z)\hat{z}}{T_1} - \frac{(M_x x + \hat{M}_y \hat{y})}{T_2}$$

or

$$\frac{d\boldsymbol{M}}{dt} = \frac{(M_0 - M_z)\hat{z}}{T_1} - \frac{(M_x x + \hat{M}_y \hat{y})}{T_2} + M_y \Delta\omega \hat{x} - M_x \Delta\omega \hat{y} + M_z \omega_1 \hat{y} - M_y \omega_1 \hat{z}$$

which is equivalent to the set of differential equations:

$$\frac{dM_x}{dt} = \frac{1}{T_2} M_x + \Delta\omega M_y$$

$$\frac{dM_y}{dt} = -\Delta\omega M_x - \frac{1}{T_2} M_y + \omega_1 M_z$$

$$\frac{dM_z}{dt} = -\omega_1 M_y - \frac{1}{T_1} M_z + \frac{M_0}{T_1}$$

These linear combinations can be expressed in the equivalent matrix forms:

$$\dot{\boldsymbol{M}} = A \cdot \boldsymbol{M} + \boldsymbol{C}$$

$$\boldsymbol{M} = \begin{pmatrix} M_x^a \\ M_y^a \\ M_z^a \end{pmatrix}$$

$$\boldsymbol{C} = \begin{pmatrix} 0 \\ 0 \\ \frac{M_0}{T_1} \end{pmatrix}$$

$$A = \begin{pmatrix} -\frac{1}{T_2} & -\Delta\omega & 0 \\ \Delta\omega & -\frac{1}{T_2} & -\omega_1 \\ 0 & \omega_1 & -\frac{1}{T_1} \end{pmatrix}$$

or

$$\dot{\boldsymbol{M'}} = A'\boldsymbol{M'}$$

$$\boldsymbol{M'} = \begin{pmatrix} 1 \\ M_x^a \\ M_y^a \\ M_z^a \end{pmatrix}$$

$$A' = \begin{pmatrix} 0 & 0 & 0 & 0 \\ 0 & -\frac{1}{T_2} & -\Delta\omega & 0 \\ 0 & \Delta\omega & -\frac{1}{T_2} & -\omega_1 \\ \frac{M_0}{T_1} & 0 & \omega_1 & -\frac{1}{T_1} \end{pmatrix}$$

If the RF pulse is described with an x and a y component (phase modulated pulses), additional terms are added.

$$A'' = \begin{pmatrix} 0 & 0 & 0 & 0 \\ 0 & -\frac{1}{T_2} & -\Delta\omega & \omega_2 \\ 0 & \Delta\omega & -\frac{1}{T_2} & -\omega_1 \\ \frac{M_0}{T_1} & -\omega_2 & \omega_1 & -\frac{1}{T_1} \end{pmatrix}$$

The second formulation, in the homogeneous matrix form, is the most elegant, as the analytical solution is readily given (for constant A').

$$\boldsymbol{M}(t) = exp(A' \cdot t)\boldsymbol{M}(0)$$

Appendix B

Summary on: MRI CEST at 1T with large μ_{eff} Ln^{3+} complexes. Tm^{3+}-HPDO3A: an efficient MRI pH reporter.

This page is required by the TUM-GS rules for a cumulative thesis.

Chemical exchange saturation transfer (CEST) is a contrast generating MRI technique based on chemically shifted protons in constant exchange with protons from water. The chemical shift is due to the protons being covalently bound to molecules other than water, and therefore subject to a different electromagnetic environment. Most chemical shifts are limited in magnitude, so that a high Larmor frequency separation can only be achieved at high external magnetic field strenghts. Accordingly, CEST mostly developed for ultra high field (UHF) and HF environments (>3 T). At high field, the paramagnetic chemical shifts are exceptionally large. This is an advantage for a selected number of applications. However, tissue heating on one hand, and paramagnetic T_1 shortening on the other, make UHF a suboptimal environment for paraCEST research, precluding many possibilities the field has to offer. It was demonstrated, theoretically and experimentally, how lower fields are advantageous to the development of paraCEST contrast agents if a realistic clinical application is envisioned. This was done experimentally by screening some available and safe to use paraCEST compounds and performing in vitro tests to determine their potential for in vivo use. Lastly, the most promising compound, Tm-HPDO3A, was characterized in depth for use as a pH-mapping agent. The characterization included: ratiometric calibration curves at different temperatures, the assessment of signal sensitivity at various B_0 fields, the choice of the best imaging sequence parameters. Finally the agent was used in vivo to image pH, achieving good results and being validated by the urine pH measured with a standard pH electrode.

The PhD candidate independently performed the steps following the paraCEST compound screening, including in vitro imaging and the rat animal experiments as well as writing the paper in its entirety.

Appendix C

Summary on: Gradient Ascent Pulse Engineering for Rapid Exchange Saturation Transfer

This page is required by the TUM-GS rules for a cumulative thesis.

ParaCEST makes use of rapid exchange rates that would, with moderate chemical shifts, lead to CEST (Z) signal coalescence. These exchange rates are catalyzed by the pH of the micromilieu, and vary considerably in the pH range of biological interest. With the intention of investigating the best achievable contrast generation for pH-mapping under SAR constraints, optimal control theory was used and adapted to the Yb-HPDO3A paraCEST agent. The microscopical parameters were determined by fitting variable amplitude same energy comparison (VASEC) plots to a three pool Bloch-McConnell CEST model. The plots were acquired at different pH, to which the exchange rates of the compound are very sensitive. These plots also give a qualitative assessment of the best amplitude (block pulse) to use for the saturation at a given total pulse energy. With the microscopic parameters determined, the optimal pulses were obtained from the CEST-adapted GRAPE algorithm. The pulses were tested experimentally, confirming the gains in saturation transfer efficiency. As the optimal pulses are dependent on the exchange rates, the pH sensitivity can be optimized for as well as the ST. For this purpose, different pulses can be optimized for the two diastereomers. The procedure, initially performed on a 600 MHz spectrometer, was then applied in the imaging environment on a 3 T clinical scanner with pulsed CEST.

The PhD candidate performed all the named steps (algorithm adaptation, simulations, pulse optimization, experimental work, pulse programming), and wrote the paper in its entirety.

Bibliography

[1] Henkelman RM, Stanisz GJ, Graham SJ. Magnetization transfer in MRI: a review. *NMR Biomed.*, 2001, 14, 57-64.

[2] Wolff SD, Balaban RS. Magnetization transfer contrast (MTC) and tissue water proton relaxation in vivo. *Magn. Reson. Med.*, 1989, 10, 135-144.

[3] Henkelman RM, Huang X, Xiang Q-S, Stanisz GJ, Swanson SD. Quantitative interpretation of magnetization transfer. *Magn. Reson. Med.*, 1993, 29, 759-766.

[4] Ceckler TL, Balaban RS. Tritium-proton magnetization transfer as a probe of cross-relaxation in acqueous lipid bilayer suspensions. *J. Magn. Reson.*, 1991, 93, 572-588.

[5] van Zijl PCM, Yadav NN. Chemical exchange saturation transfer (CEST): What is in the name and what isn't? *Magn. Reson. Med.*, 2011, 65, 927-948.

[6] Jin T, Kim SG. In vivo saturation transfer imaging of nuclear overhauser effect from aromatic and aliphatic protons: implications to APT quantification. *Proc. ISMRM 21st Annu. Meeting. 2013*, pp. 2528.

[7] Zaiss M, Bachert P. Chemical exchange saturation transfer (CEST) and MR Z-spectroscopy in vivo: a review of theoretical approaches and methods. *Phys. Med. Biol.*, 2013, 58, 221-269.

[8] McConnell HM. Reaction rates by nuclear magnetic resonance. *J. Chem. Phys.*, 1958, 28, 430.

[9] Morrison C, Henkelmann RM. A model for magnetization transfer in tissues. *Magn. Reson. Med.*, 1995, 33, 475-482.

[10] Ward KM , Aletras AH, Balaban RS. A new class of contrast agents for MRI based on proton chemical exchange dependent saturation transfer (CEST). *J. Magn. Reson.*, 2000, 143, 79-87.

[11] Sun PZ, van Zijl PCM, Zhou J. Optimization of the irradiation power in chemical exchange dependent saturation transfer experiments. *J. Magn. Reson.*, 2005, 175, 193-200.

[12] Zhou J, van Zijl PCM. Chemical exchange saturation transfer imaging and spectroscopy. *Prog. Nucl. Magn. Reson. Spectrosc.*, 2006, 48, 109-136.

[13] McMahon MT, Gilad AA, Zhou J, Sun PZ, Bulte JWM, van Zijl PCM. Quantifying exchange rates in chemical exchange saturation transfer agents using the saturation time and saturation power dependencies of the magnetization transfer effect on the magnetic resonance imaging signal (QUEST and QUESP): Ph calibration for poly-L-lysine and a starburst dendrimer. *Magn. Reson. Med.*, 2006, 55, 836-847.

[14] Zu ZL, Janve VA, Li K, Does MD, Gore JC, Gochberg DF. Multi-angle ratiometric approach to measure chemical exchange in amide proton transfer imaging. *Magn. Reson. Med.*, 2012, 68, 711–719.

[15] Zu ZL, Janve VA, Xu JZ, Does MD, Gore JC, Gochberg DF. A new method for detecting exchanging amide protons using chemical exchange rotation transfer. *Magn. Reson. Med.*, 2013, 69, 637–647.

[16] Zu ZL, Xu J, Li H, Chekmenev EY, Quarles CC, Does MD, Gore JC, Gochberg DF. Imaging amide proton transfer and nuclear overhauser enhancement using chemical exchange rotation transfer (CERT). *Magn. Reson. Med.*, 2014, 72(2), 471-476.

[17] Friedman JI, McMahon MT, Stivers JT, van Zijl PC. Indirect detection of labile solute proton spectra via the water signal using frequency-labeled exchange (FLEX) transfer. *J. Am. Chem. Soc.*, 2010, 132, 1813–1815.

[18] Lin CY, Yadav NN, Ratnakar J, Sherry AD, van Zijl PC. In vivo imaging of paraCEST agents using frequency labeled exchange transfer MRI. *Magn. Reson. Med.*, 2014, 71(1), 286-293.

[19] Yadav NN, Jones CK, Hua J, Xu J, van Zijl PC. Imaging of endogenous exchangeable proton signals in the human brain using frequency labeled exchange transfer imaging. *Magn. Reson. Med.*, 2013, 69(4), 966-973.

[20] Zaiss M, Bachert P. Exchange-dependent relaxation in the rotating frame for slow and intermediate exchange – modeling off-resonant spin-lock and chemical exchange saturation transfer. *NMR Biomed.*, 2013, 26(5), 507-518.

[21] Roeloffs V, Meyer C, Bachert P, Zaiss M. Towards quantification of pulsed spinlock and CEST at clinical MR scanners: an analytical interleaved saturation-relaxation (ISAR) approach. *NMR Biomed.*, 2015, 28(1), 40-53.

[22] Terreno E, Delli Castelli D, Aime S. Encoding the frequency dependence in MRI contrast media: the emerging class of CEST agents. *Contrast Media Mol. Imaging*, 2010, 5, 78-98.

[23] Walker-Samuel S, Ramasawmy R, Torrealdea F, Rega M, Rajkumar V, Johnson SP, Richardson S, Goncalves M, Parkes HG, Arstad E, Thomas DL, Pedley RB, Lynthgoe MF, Golay X. In vivo imaging of glucose uptake and metabolism in tumors. *Nat. Med.*, 2013, 19(8), 1067-1072.

[24] Longo DL, Dastrù W, Digilio G, Keupp J, Langereis S, Lanzardo S, Prestigio S, Steinbach O, Terreno E, Uggeri F, Aime S. Iopamidol as a responsive MRI-Chemical exchange saturation transfer contrast agent for pH mapping of kidneys: in vivo studies in mice at 7T. *Magn. Reson. Med.*, 2011, 65, 202-211.

[25] Chen LQ, Howison CM, Jeffery JJ, Robey IF, Kuo PH, Pagel MD. Evaluations of extracellular pH within in vivo tumors using acidoCEST MRI. *Magn. Reson. Med.*, 2014, 72, 1408-1417.

[26] Chan KW, Bulte JW, McMahon MT. Diamagnetic chemical exchange saturation transfer (diaCEST) liposomes: physicochemical properties and imaging applications. *Wiley Interdiscip. Rev. Nanomed. Nanobiotechnol.*, 2014, 6(1), 111-124.

[27] Keltner JR, Carlson JW, Roos MS, Wong STS, Wong TL, Budinger TF. Electromagnetic Fields of Surface Coil in Vivo NMR at High Frequencies. *Magn Reson Med.*, 1991, 22, 467-480.

[28] Woessner DE, Zhang S, Merritt ME, Sherry AD. Numerical solution of the Bloch equations provides insights into the optimum design of PARACEST agents for MRI. *Magn. Reson. Med.*, 2005, 53(4), 790-9.

[29] Olatunde AO, Cox JM, Daddario MD, Spernyak JA, Benedict JB, Morrow JR. Seven-coordinate Co(II), Fe(II) and six-coordinate Ni(II) amide-appended macrocyclic complexes as paraCEST agents in biological media. *Inorg. Chem.*, 2014, 53, 8311-8321.

[30] Schroeder L, Lowery TJ, Hilty C, Wemmer DE, Pines A. Molecular imaging using a targeted magnetic resonance hyperpolarized biosensor. *Science*, 2006, 314, 446-449.

[31] Guenther D, Hanisch G, Kauczor HU. Functional MR imaging of pulmonary ventilation

using hyperpolarized noble gases. *Acta Radiol.*, 2000, 41(6), 519-528.

[32] Spence MM, Rubin SM, Dimitrov IE, Ruiz EJ, Wemmer DE, Pines A, Yao SQ, Tian F, Schultz PG. Functionalized Xenon as a biosensor. *Proc. Nat. Acad. Sci. USA*, 2001, 98(19), 10654-10657.

[33] Delli Castelli D, Terreno E, Longo D, Aime S. Nanoparticle-based chemical exchange saturation transfer (CEST) agents. *NMR Biomed.*, 2013, 26, 839-849.

[34] Terreno E, Delli Castelli D, Milone L, Rollet S, Stancanello J, Violante E, Aime S. First ex-vivo MRI co-localization of two LIPOCEST agents. *Contrast Media Mol. Imaging*, 2008, 3, 38-43.

[35] Terreno E, Delli Castelli D, Violante E, Sanders HM, Sommerdijk NA, Aime S. Osmotically shrunken LIPOCEST agents: an innovative class of magnetic resonance imaging contrast media based on chemical exchange saturation transfer. *Chemistry*, 2009, 15(6), 1440-1448.

[36] Perrin CL. Proton exchange in amides: surprises from simple systems. *Acc. Chem. Res.*, 1989, 22, 268-275.

[37] Liepinsh E, Otting G. Proton exchange rates from amino acid side chains - implications for image contrast. *Magn. Reson. Med.*, 1996, 35(1), 30-42.

[38] Liu G, Gilad AA, Bulte JWM, van Zijl PCM, McMahon MT. High throughput screening of chemical exchange saturation transfer MR contrast agents. *Contrast Media Mol. Imaging*, 2010, 5(3), 162-170.

[39] Liu G, Song X, Chan KWY, McMahon MT. Nuts and bolts of chemical exchange saturation transfer MRI. *NMR Biomed.*, 2013, 26(7), 386-391.

[40] Zaiss M, Xu J, Goerke S, Khan IS, Singer RJ, Gore JC, Gochberg DF, Bachert P. Inverse Z spectrum analysis for spillover-, MT-, and T_1-corrected steady-state pulsed CEST-MRI - application to pH-weighted MRI of acute stroke. *NMR Biomed.*, 2014, 27, 240-252.

[41] Hanahan D, Weinberg RA. Hallmarks of cancer: the next generation. *Cell*, 2011, 144, 646-674.

[42] Semenza GL. Tumor metabolism: cancer cells give and take lactate. *J. Clin. Invest.*, 2008, 118(12), 3835-3837.

[43] Gillies RJ, Raghunand N, Karczmar GS, Bhujwalla ZM. MRI of the tumor microenvironment. *J. Magn. Reson. Imaging*, 2002, 16(4), 430-450.

[44] Golman K, in't Zandt R, Lerche M, Pehrson R, Ardenkjaer-Larsen JH. Metabolic imaging by hyperpolarized 13C magnetic resonance imaging for in vivo tumor diagnosis. *Cancer Res.*, 2006, 66, 10855-10860.

[45] Gallagher FA, Kettunen MI, Day SE, Hu DE, Ardenkjaer-Larsen JH, in 't Zandt R, Jensen PR, Karlsson M, Golman K, Lerche MH, Brindle KM. Magnetic resonance imaging of pH in vivo using hyperpolarized 13C-labelled bicarbonate. *Nature*, 2008, 453(7197), 940-943.

[46] Scholz DJ, Janich MA, Köllisch U, Schulte RF, Ardenkjaer-Larsen JH, Frank A, Haase A, Schwaiger M, Menzel MI. Quantified pH imaging with hyperpolarized 13C-bicarbonate. *Magn. Reson. Med.*, 2014, doi: 10.1002/mrm.25357 (preprint).

[47] Stubbs M, Bhujwalla ZM, Toyer GM, Rodriguez LM, Maxwell RJ, Morgan R, Howe FA, Griffiths JR. An assessment of 31P MRS as a method of measuring pH in rat tumours. *NMR Biomed.*, 1992, 5(6), 351-359.

[48] Gillies RJ, Liu Z, Bhujwalla Z. 31P-MRS measurements of extracellular pH of tumors using 3-aminopropylphosphonate. *Am. J. Physiol.*, 1994, 267, C195-203.

[49] Kim M, Gillen J, Landman BA, Zhou J, van Zijl CM. Water saturation shift referencing

(WASSR) for chemical exchange saturation transfer (CEST) experiments. *Magn. Reson. Med.*, 2009, 61(6), 1441-1450.

[50] Forsen S, Hoffman RA. Study of moderately rapid chemical exchange reaction by means of nuclear magnetic double resonance. *J. Chem. Phys.*, 1963, 39, 2892-2901.

[51] Ward KM, Balaban RS. Determination of pH using water protons and chemical exchange dependent saturation transfer (CEST). *Magn. Reson. Med.*, 2000, 44(5), 799-802.

[52] Funk AM, Fries PH, Harvey P, Kenwright AM, Parker D. Experimental measurement and theoretical assessment of fast lanthanide electronic relaxation in solution with four series of isostructural complexes. *J. Phys. Chem. A*, 2013, 117, 905-917.

[53] Clore GM, Iwahara J. Theory, practice, and applications of paramagnetic relaxation enhancement for the characterization of transient low-population states of biological macromolecules and their complexes. *Chem. Rev.*, 2009, 109, 4108-4139.

[54] Aime S, Barge A, Delli Castelli D, Fedeli F, Mortillaro A, Nielsen FU, Terreno E. Paramagnetic lanthanide (III) complexes as pH-sensitive chemical exchange saturation transfer (CEST) contrast agents for MRI applications. *Magn. Reson. Med.*, 2002, 47, 639-648.

[55] van Zijl PCM, Jones CK, Ren J, Malloy CR, Sherry AD. MRI detection of glycogen in vivo by using chemical exchange saturation transfer imaging (glycoCEST). *Proc. Natl. Acad. Sci. U.S.A.*, 2007, 104(11), 4359-4364.

[56] Haris M, Singh A, Cai K, Kogan F, McGarvey J, DeBrosse C, Zsido GA, Witschey WRT, Koomalsingh K, Pilla JJ, Chirinos JA, Ferrari VA, Gorman JH, Hariharan H, Gorman RC, Reddy R. A technique for in vivo mapping of myocardial creatine kinase metabolism. *Nat. Med.*, 2014, 20(2), 209-214.

[57] Delli Castelli D, Ferrauto G, Cutrin JC, Terreno E, Aime S. In vivo maps of extracellular pH in murine melanoma by CEST-MRI. *Magn. Reson. Med.*, 2014, 71(1), 326-332.

[58] Sheth VR, Li Y, Chen LQ, Howison CM, Flask CA, Pagel MD. Measuring in vivo tumor pHe with CEST-FISP MRI. *Magn. Reson. Med.*, 2012, 67(3), 760-768.

[59] Longo DL, Sun PZ, Consolino L, Michelotti FC, Uggeri F, Aime S. A general MRI-CEST ratiometric approach for pH imaging: demonstration of in vivo pH mapping with Iobitridol. *J. Am. Chem. Soc.*, 2014, 136, 14333-14336.

[60] Chan KWY, Liu G, Song X, Kim H, Yu T, Arifin DR, Gilad AA, Hanes J, Walczak P, van Zijl PCM, Bulte JWM, McMahon MT. MRI-detectable pH nanosensors incorporated into hydrogels for in vivo sensing of transplanted-cell viability. *Nat. Mat.*, 2013, 12, 268-275.

[61] Chan KW, Yu T, Qiao Y, Liu Q, Yang M, Patel H, Liu G, Kinzler KW, Vogelstein B, Bulte JW, van Zijl PC, Hanes J, Zhou S, McMahon MT. A diaCEST MRI approach for monitoring liposomal accumulation in tumors. *J. Control. Release*, 2014, 180, 51-59.

[62] Flament J, Geffroy F, Medina C, Robic C, Mayer JF, Meriaux S, Valette J, Robert P, Port M, Le Bihan D, Lethimonnier F, Boumezbeur F. In vivo CEST MR imaging of U87 mice brain tumor angiogenesis using targeted LipoCEST contrast agent at 7T. *Magn. Reson. Med.*, 2013, 69(1), 179-187.

[63] Aime S, Delli Castelli D, Terreno E. Highly sensitive MRI chemical exchange saturation transfer agents using liposomes. *Angew. Chem. Int. Ed.*, 2005, 44(34), 5513-5515.

[64] Kogan F, Hariharan H, Reddy R. Chemical exchange saturation transfer (CEST) imaging: description of technique and potential clinical applications. *Curr. Radiol. Rep.*, 2013, 1, 102-114.

[65] Müller-Lutz A, Khalil N, Schmitt B, Jellus V, Pentang G, Oeltzschner G, Antoch G, Lanzman RS, Wittsack HJ. Pilot study of iopamidol-based quantitative pH imaging on a

clinical 3T MR scanner. *MAGMA*, 2014, 27(6), 477-485.

[66] Kogan F, Singh A, Debrosse C, Haris M, Cai K, Nanga RP, Elliott M, Hariharan H, Reddy R. Imaging of glutamate in the spinal cord using gluCEST. *Neuroimage*, 2013, 77, 262-267.

[67] Ling W, Regatte RR, Navon G, Jerschow A. Assessment of glycosaminoglycan concentration in vivo by chemical exchange-dependent saturation transfer (gagCEST). *Proc. Natl. Acad. Sci. U.S.A.*, 2008, 105(7), 2266-2270.

[68] Haris M, Cai K, Singh A, Hariharan H, Reddy R. In vivo mapping of brain myo-inositol. *Neuroimage*. 2011, 54(3), 2079-2085.

[69] Kogan F, Haris M, Singh A, Cai K, Debrosse C, Nanga RP, Hariharan H, Reddy R. Method for high-resolution imaging of creatine in vivo using chemical exchange saturation transfer. *Magn. Reson. Med.*, 2014, 71(1), 164-172.

[70] Zhou J, Blakeley JO, Hua J, Kim M, Laterra J, Pomper MG, van Zijl PCM. Practical data acquisition method for human brain tumor amide proton transfer (APT) imaging. *Magn. Reson. Med.*, 2008, 60(4), 842-849.

[71] Wen Z, Hu S, Huang F, Wang X, Guo L, Quan X, Wans S, Zhou J. MR imaging of high-grade brain tumors using endogenous protein and peptide-based constrast. *Neuroimage*, 2010, 51(2), 616-622.

[72] Togao O, Yoshiura T, Keupp J, Hiwatashi A, Yamashita K, Kikuchi K, Suzuki Y, Suzuki SO, Iwaki T, Hata N, Mizoguchi M, Yoshimoto K, Sagiyama K, Takahashi M, Honda H. Amide proton transfer imaging of adult diffuse gliomas: correlation with histopathological grades. *Neuro Oncol.*, 2014, 16(3), 441-448.

[73] Tietze A, Blicher J, Mikkelsen IK, stergaard L, Strother MK, Smith SA, Donahue MJ. Assessment of ischemic penumbra in patients with hyperacute stroke using amide proton transfer (APT) chemical exchange saturation transfer (CEST) MRI. *NMR Biomed.*, 2014, 27(2), 163-174.

[74] Schmitt B, Zamecnik P, Zaiss M, Rerich E, Schuster L, Bachert P, Schlemmer HP. A new contrast in MR mammography by means of chemical exchange saturation transfer (CEST) imaging at 3 Tesla: preliminary results. *Rofo.*, 2011, 183(11), 1030-1036.

[75] Li C, Peng S, Wang R, Chen H, Su W, Zhao X, Zhou J, Chen M. Chemical exchange saturation transfer MR imaging of Parkinson's disease at 3 Tesla. *Eur. Radiol.*, 2014, 24, 2631-2639.

[76] Dula AN, Arlinghaus LR, Dortch RD, Dewey BE, Whisenant JG, Ayers GD, Yankeelov TE, Smith SA. Amide proton transfer imaging of the breast at 3T: establishing reproducibility and possible feasibility assessing chemotherapy response. *Magn. Reson. Med.*, 2012, 70, 216-224.

[77] Paech D, Zaiss M, Meissner JE, Windschuh J, Wiestler B, Bachert P, Neumann JO, Kickingereder P, Schlemmer HP, Wick W, Nagel AM, Heiland S, Ladd, ME, Bendszus M, Radbruch A. Nuclear overhauser enhancement mediated chemical exchange saturation transfer imaging at 7 tesla in glioblastoma patients. *PLoS One*, 2014, 9(8), e104181.

[78] Trott O, Palmer AG. $R_{1\rho}$ relaxation outside of the fast-exchange limit. *J. Magn. Reson.*, 2002, 154, 157-160.

[79] Sun PZ, Benner T, Kumar A, Sorensen AG. Investigation of Optimizing and Translating pH-Sensitive Pulsed -Chemical Exchange Saturation Transfer (CEST) Imaging to a 3T Clinical Scanner. *Magn. Reson. Med.*, 2008, 60, 834-841.

[80] Dixon WT, Hancu I, Ratnakar SJ, Sherry AD, Lenkinski RE, Alsop DC. A multislice

gradient echo pulse sequence for CEST imaging. *Magn. Reson. Med.*, 2010, 63(1), 253-256.

[81] Delli Castelli D, Terreno E, Cabella C, Chaabane L, Lanzardo S, Tei L, Visigalli M, Aime S. Evidence for in vivo macrophage mediated tumor uptake of paramagnetic/fluorescent liposomes. *NMR Biomed.*, 2009, 22(10), 1084-1092.

[82] Haacke EM, Brown RW, Thompson MR, Venkatesan R. Magnetic Resonance Imaging: Physical Principles and Sequence Design. 1999, John Wiley and Sons (Hoboken, N.J.), pp. 51-63.

Afterword

The following is a personal statement on the broader PhD project.

In 2012 we set out to test the clinical translatability of some very interesting pH-sensitive CEST compounds. Clinical interest in pH-mapping was high, with Prof. Schwaiger involved in pursuing different strategies to achieve it, and willing to provide the instrumentation and setting to investigate clinical translation potential. Molecular imaging expert Prof. Aime provided some promising CEST compounds that had been tested in his lab both *in vitro* and on small animals. However, despite the elegance of the ratiometric approach to overcome concentration-dependence, and the usefulness of pH as a tumoral marker, some key limitations were overlooked.

Firstly, there is a mismatch between a demanding data analysis and a low-sensitivity technique. Among imaging modalities, MRI does not possess a high sensitivity. Moreover, the CEST technique itself generates little contrast even on abundant endogenous proton pools. The use of contrast agents limits the availability of exchanging spins necessary to generate CEST signal. A ratio of two CEST signals needs to be performed to reach concentration-independence. An excellent SNR is crucial to reach acceptable pH sensitivity after error propagation.

Secondly, differences in safety limits for RF energy deposition between preclinical and clinical instruments are much larger than previously envisioned.

The mentioned limitations presented themselves early on, at the first in vitro CEST experiments with Yb-HPDO3A on a clinical 3T MRI scanner. Coming from a strictly preclinical or even spectroscopical environment, there was not a clear idea of how big the sensitivity requirements were. Acknowledging a lack in both signal sensitivity and in-depth understanding of the theoretical framework, it was decided to take a step back and define the highest achievable paraCEST signal on the clinical instrument. This was done with the help of Prof. Glaser's expertise on pulse design using optimal control algorithms.

In parallel, a project for an animal study was written to provide the confirmation of in vivo pH mapping with clinical hardware. The arrival of a high-field preclinical system (with the DNP-polarizer) opened the way to further projects. An additional goal became the comparison of CEST pH-maps in the tumor with ^{13}C hyperpolarized techniques mapping the pyruvate metabolism (for imaging the Warburg effect) and pH (for cross-validation).

CEST pulse optimization produced good results, but the signal increases where at least one order of magnitude below what would have been required to translate Yb-HPDO3A paraCEST to clinical hardware. This prompted a change of the animal study's ethics proposal to use on preclinical instrumentation only.

Instead, the diaCEST contrast agent Iopamidol was investigated for use on clinical hardware. Results from high concentration solutions in vitro and in vivo (bladder) on clinical hardware had already been published. At the highest in vivo concentration recorded for iopamidol in tumors (5 mM), a sensitivity assessment was performed. No sufficient contrast generation was obtained for quantification of pH (both using two-pool or two-pulse ratiometric analyses).

On the preclinical 7T scanner, some hardware limitations were found that would hamper paraCEST measurements. The maximum amplitude for the CEST presaturation was approximately 7 μT, which proved insufficient for our purposes. The tumoral biodistribution of iopamidol was found to be in line with recorded CT data on murine tumor models, but much worse on rat tumor models. The main issue is thought to be the size of the rat tumors under investigation. As large rat tumors are a requirement for accurate ^{13}C analyses due to limited spatial resolution, the iopamidol pH-mapping was ultimately dropped in favour of endoCEST.

The use of contrast agents for CEST does not show particular promise. In a field where the endogenous signals are (at the current state of scientific research) difficult to assess - let alone quantify - contrast agents will struggle to find a realistic clinical application. This is particularly true for contrast agents that were not specifically designed for CEST (the HPDO3A ligand was developed for relaxation enhancers and Iopamidol as a CT contrast agent). However, accurately designed paraCEST agents for low-field applications - combined with biotechnological solutions - might well prove to be viable clinically.

I will conclude this personal statement by thanking Prof. Aime for giving me the possibility to conduct cutting edge research, Prof. Schwaiger for supporting me and for allowing a high degree of independence, as well as Prof. Glaser for his crucial theoretical guidance in this highly interdisciplinary field.

In addition to the co-authors, I would like to thank the following people for moral and/or technical support (in alphabetical order):

Bianchi Patrick, Bieth Marie, Cabello Jorge, Cervantez Barbara, Christophe Meyer, Consolino Lorena, Dastrù Walter, Di Gregorio Enza, Dregely Isabel, Durst Markus, Düwel Stephan, Farrell Eliane, Fauner Thomas, Ferrauto Giuseppe, Ferry Pauline, Feuerecker Benedikt, Filippi Miriam, Fuersich Benjamin, Fürst Sebastian, Garon Ariane, Gringeri Concetta, Hehn Nicholas, Heydenreich Thomas, Hundshammer Christian, Kallies Wolfgang, Khegai Oleksandr, Köllisch Ulrich, Kubala Eugen, Kudielka Guido, Kunze Karl, Laitinen Iina, Lapert Marc, Liu Xin, Longo Dario, Lukas Mathias, Marx Raimund, Menini Anne, Michalik Michael, Michelotti Filippo, Molina Miguel, Munoz Kim, Omidvari Negar, Pagoto Amerigo, Pariani Giorgio, Rincon Teresa, Schachoff Sylvia, Schilling Franz, Scholz Johannes, Schröder Albert, Schulte-Herbrüggen Thomas, Schulte Rolf, Solana Ana Beatriz, Somlai Ian, Sprenger Tim, Tesch Michael, Topping Geoffrey, Voelchert Anna, Wu Mingming.